

**IMPEDANCE CHARACTERIZATION OF POROUS CARBON
ELECTRODES WITH CONTROLLED PORE SIZE DISTRIBUTION:
EXPERIMENTAL VERIFICATION**

by

Trishank Sharma

B.Tech., Indian Institute of Technology, Roorkee, 2015

A THESIS SUBMITTED IN PARTIAL FULFILLMENT OF
THE REQUIREMENTS FOR THE DEGREE OF

MASTER OF APPLIED SCIENCE

in

THE FACULTY OF GRADUATE AND POSTDOCTORAL STUDIES
(Chemical and Biological Engineering)

THE UNIVERSITY OF BRITISH COLUMBIA

(Vancouver)

February 2019

© Trishank Sharma, 2019

The following individuals certify that they have read, and recommend to the Faculty of Graduate and Postdoctoral Studies for acceptance, a thesis entitled:

Impedance Characterization of Porous Carbon Electrodes with Controlled Pore Size Distribution: Experimental Verification

submitted by Trishank Sharma in partial fulfillment of the requirements for
the degree of Master of Applied Science
in Chemical and Biological Engineering

Examining Committee:

Dr. Walter Mérida, Mechanical Engineering
Supervisor

Dr. Madjid Mohseni, Chemical and Biological Engineering
Supervisory Committee Member

Dr. Heather Trajano, Chemical and Biological Engineering
Supervisory Committee Member

Abstract

In this work, electrochemical impedance spectroscopy (EIS) measurements were carried out on an increasingly complex distribution of cylindrical pores with well-defined geometries. The desired pores were made via drilling on graphite surfaces. The pore structure complexity was gradually increased starting with the evaluation of single pore impedances followed by drilling multiple pores with uniform pore dimensions and finally generating pore size distributions (PSD) having distributed pore radii or depth or a combination of both. The impedance response was interpreted using ZView fitting and a graphical approach and was found to be well described by the existing theory. The impedance response of the resulting porous electrodes was characterised with varying geometrical and electrochemical parameters - pore depth, pore radii, pore density, and electrolyte conductivity. The obtained results suggest a possibility to use measurements on drilled cylindrical pores to interpret more complex PSD as measurements of PSD were successfully modelled by adding the impedance response of single pores.

Lay Summary

Porous materials are widely used either as electrodes or to promote mass transport, for example in fuel cells and supercapacitors. The porosity of a material influences the overall performance, and Electrochemical Impedance Spectroscopy (EIS) is one of the very few techniques that is sensitive to the pore geometry. Although EIS is sensitive to pore geometries, the impedance response for non-uniform pore arrays in porous materials is hard to understand due to the wide pore size distributions. In this thesis, an experimental framework is demonstrated to verify the impedance spectra for progressively more complex pore size distributions with well-defined structure. Pore arrays, both of uniform pore dimensions and non-uniform pore dimensions can be successfully represented as a sum of experimental responses of single pores. This approach can be used to verify the pore impedance for non-uniform ordered pore arrays with well-defined geometry.

Preface

This dissertation is submitted for the degree of Master of Applied Science at The University of British Columbia. The materials presented in this thesis, including the literature review, experimental work, data analysis, and thesis preparation, was completed by Trishank Sharma under the supervision of Professor Walter Mérida at the Clean Energy Research Centre, the University of British Columbia. Dr. Thomas Holm and Dr. Jesus Adrian Diaz Real provided guidance in the conception of experimental plans and data interpretation.

The following manuscript has been communicated in academic journal.

- T. Sharma, T. Holm, J.A. Diaz-Real, W. Mérida, “Experimental Verification of Pore Impedance Theory: Drilled Graphite Electrodes with Gradually More Complex Pore Size Distribution”. (Under Review)

The work has been presented by the author at the following conference:

- T. Sharma, J. A. Diaz-Real, T. Holm, B. Zahiri, and W. Mérida, “Pore Impedance: Experimental Verification of Transmission Line Model on Porous Carbon Electrodes with Gradually More Complex Geometric Systems” 7th Annual ECS BC Young Electrochemists Symposium. (2018)

Table of Contents

Abstract	iii
Lay Summary	iv
Preface	v
Table of Contents	vi
List of Tables	ix
List of Figures	x
Nomenclature	xiii
List of Abbreviations	xv
Acknowledgements	xvi
1 Introduction	1
1.1 Research Background and Motivation	1
1.2 Impedance of porous electrodes	3
1.2.1 Electric double layer	3
1.2.2 Electrochemical Impedance Spectroscopy (The technique)	4
1.2.3 Equivalent Electrical Circuit	5
1.2.4 Impedance of cylindrical pores	6
1.2.5 Transmission Line Equivalent Circuit Model	8
1.2.6 Influence of Pore Geometry on Impedance	9
1.2.7 Impedance Spectroscopy for Porosimetry Studies	10
1.3 Significance	10
1.4 Objectives	11
1.5 Thesis Layout	12

2	Experimental Systems and Experimental Methods	13
2.1	Sample Preparation	13
2.1.1	Preparation of Glassy Carbon Samples	13
2.2.2	Preparation of Graphite Samples	14
2.2	Experimental Setup	14
2.3	Electrochemical Characterization	16
2.4	Surface Characterization	19
2.5	EIS Data Interpretation	20
2.5.1	ZView Fitting (1 st approach)	20
2.5.2	Graphical Method (2 nd approach)	22
3	Results	24
3.1	Initial Trials on Glassy Carbon Samples	24
3.2	Verification of Pore Geometry (Graphite Samples)	28
3.3	Selection of Electrolyte	30
3.4	Pore Depth Variation	31
3.5	Pore Radii Variation	37
3.6	Uniform Pore Arrays (Uniform Pore Radii & Depth)	42
3.7	Effect of Electrolyte and Conductivity	44
3.8	Pore Size Distributions (PSD)	50
3.9	Comment on the nature of CPE behaviour	53
4	Conclusions and Future Work	55
4.1	Conclusions	55
4.2	Recommendations for Future Work	55

Bibliography

56

List of Tables

Table 1.1: Impedance of Common Electrical Elements	5
Table 2.1: Summary of the experimental framework.....	18
Table 3.1: Change of the pore depth on transition frequency.....	32
Table 3.2: Comparison of electrochemical parameters by ZView (Method 1 / M1) and Graphical approach (Method 2 / M2) for same pore diameter (0.74 mm) and varying pore depth	33
Table 3.3: Change of the pore radii on transition frequency	38
Table 3.4: Comparison of electrochemical parameters by ZView (Method 1 / M1) and Graphical approach (Method 2 / M2) for same pore depth (5.20 mm) and varying pore radii	39
Table 3.5: Summary of electrochemical parameters for varying electrolyte conductivity ...	47

List of Figures

Figure 1.1: Typical Nyquist plot for an ideal porous electrode	7
Figure 1.2: Distributed Resistance and Capacitance in a Pore Represented by the Transmission Line Model	9
Figure 2.1: Sketch of Experimental Setup	15
Figure 2.2: Schematic of Experimental Framework	19
Figure 2.3: (a) Example of fitting impedance data with ZView for a single pore, inset-high frequency data (b) Determination of $R_{\Omega,p}$ value by the graphical method for pore diameter = 0.74 mm, pore depth = 5.20 mm	21
Figure 2.4: Analysis of experimental data by graphical method (a) imaginary part of impedance vs frequency plot (b) frequency dependence of CPE parameter Q	23
Figure 3.1: Nyquist plots for experimental data of 11×11 pore array ($r = 22.5$ μm , $L = 400$ μm) in 1.1 mm \times 1.1 mm area of Glassy carbon sample for two different electrolytes	24
Figure 3.2: Nyquist plots for experimental data and ZView fitted plots of 11×11 pore array ($r = 22.5$ μm , $L = 400$ μm) in 1.1 mm \times 1.1 mm area of Glassy carbon sample	25
Figure 3.3: Equivalent circuit used to fit impedance of 11×11 pore array in 1.1 mm \times 1.1 mm area of Glassy carbon sample	26
Figure 3.4: Micro-CT scan images of 11×11 pore array in 1.1 mm \times 1.1 mm area of Glassy carbon sample (Resolution 7.4 μm / voxel side)	27
Figure 3.5: Segmented slices of the pores created by laser micromachining on Glassy carbon sample	27

Figure 3.6: Micro-CT scan images of cylindrical pores drilled on graphite piece (a) 2D image of pores with same pore diameter (0.74 mm) (b) 2D image of pores with same pore depth (5.20 mm) (c), (d) 3D images of pores with same pore diameter (0.74 mm) and varying pore depths	29
Figure 3.7: Comparison of electrolytes (a) Nyquist plots (b) Bode Plots	30
Figure 3.8: Nyquist plots for effect of varying pore depth (Single pore)	31
Figure 3.9: Pore diameter = 0.74 mm (a) Area normalized pore capacitance values vs pore depth (b) CPE parameters Q and α vs pore depth (c) Electrolyte resistance in pores vs pore depth (d) Absolute values of pore capacitance vs pore depth	34
Figure 3.10: Cyclic Voltammetry curves for pore depth variation for a single pore (Pore diameter = 0.74 mm)	36
Figure 3.11: Nyquist plots for effect of varying pore radii (Single pore)	37
Figure 3.12: Pore depth = 5.20 mm (a) Area normalized pore capacitance values vs pore radii (b) CPE parameters Q and α vs pore radii (c) Electrolyte resistance in pores vs r^{-2} (d) Absolute values of pore capacitance vs pore radii	40
Figure 3.13: Cyclic Voltammetry curves for pore radii variation for a single pore (Pore depth = 5.20 mm)	41
Figure 3.14: (a) Nyquist plots (absolute values of impedance) (b) Nyquist plots (area normalized impedance) (c) Bode Plots for uniform pore arrays	43
Figure 3.15: Cyclic Voltammetry curves for uniform pore arrays	44

Figure 3.16: Trend of (a) Electrolyte resistance in pores vs inverse of electrolyte conductivity (b) Area normalized pore capacitance values vs electrolyte conductivity (Pore diameter = 1.0 mm, Depth = 3.0 mm)	45
Figure 3.17: Nyquist Plots for effect of varying electrolyte conductivity (Single pore)	46
Figure 3.18: Cyclic Voltammetry curves for effect of varying electrolyte conductivity (single pore)	48
Figure 3.19: Nyquist plots for four cases of non-uniform pore distributions (a) 6 pore array, 2 different radii: 0.33 mm (3 pores), 0.66 mm (3 pores) (b) 6 pore array, 2 different depths: 3.8 mm (3 pores), 5.2 mm (3 pores) (c) 6 pore array, 3 different radii: 0.23 mm (2 pores), 0.33 mm (2 pores), 0.66 mm (2 pores) (d) 4 pore array, 4 different radii: 0.33 mm, 0.37 mm, 0.51 mm, 0.66 mm (1 each)	51
Figure 3.20: Nyquist plot for a non-uniform pore array: 6 pore array, 3 different radii: 0.23 mm, 0.37 mm, 0.51 mm, 2 different depths: 3.80 mm, 5.20 mm	52

Nomenclature

Symbol	Description	Unit
α	Constant phase element coefficient	--
c_i^0	Bulk electrolyte concentration	mol L ⁻¹
C_{dl}	Double layer capacitance	$\mu\text{F cm}^{-2}$
C_{pore}	Absolute capacitance of pore walls	μF
d	Double layer thickness	nm
D	Pore diameter	mm
e	Elementary charge	C
E	Potential	V
ϵ_0	Permittivity of vacuum	F m ⁻¹
ϵ_r	The dielectric constant of electrolyte	--
f	Frequency	Hz
f_t	Transition frequency	Hz
i	Current Density	$\mu\text{A cm}^{-2}$
I	Current	μA
k_B	Boltzmann constant	J K ⁻¹
K	Debye-Hückel parameter	nm ⁻¹
K	Electrolyte conductivity	$\Omega^{-1} \text{cm}^{-1}$
L	Pore depth	mm
	Inductance	H
ρ	Electrolyte resistivity	Ωcm
Q	Constant phase element parameter	$\mu\text{F cm}^{-2} \text{s}^{\alpha-1}$

Q_{flat}	Constant phase element parameter for flat part	$\mu\text{F cm}^{-2} \text{s}^{\alpha-1}$
r	Pore radii	mm
R_{sol}	Resistance offered by electrolyte outside a pore	Ω
$R_{\Omega,p}$	Resistance offered by electrolyte inside a pore	Ω
T	Temperature	K
ω	Angular frequency	rad s^{-1}
Z_i	Valency of ion i	--
Z_{CPE}	Impedance of a constant phase element	ohm
$Z_{p,i}$	Impedance of i^{th} pore	ohm
$Z_{p,\text{total}}$	Summation of impedance of single pores	ohm
Z_{pore}	Impedance of cylindrical pores	ohm
Z_t	Total impedance of a porous electrode	ohm

List of Abbreviations

Abbreviation	Description
ac	Alternating Current
CE	Counter Electrode
CNC	Computer Numerical Control
CPE	Constant Phase Element
CT	Computed Tomography
CV	Cyclic Voltammetry
DC	Direct Current
DI	Deionized
EDLC	Electric Double Layer Capacitor
EEC	Equivalent Electrical Circuit
EIS	Electrochemical Impedance Spectroscopy
GC	Glassy Carbon
IS	Impedance Spectroscopy
MIP	Mercury Intrusion Porosimetry
M1	Method 1
M2	Method 2
OCP	Open Circuit Potential
PSD	Pore Size Distribution(s)
RC	Resistor-Capacitor
RE	Reference Electrode
TLM	Transmission Line Model
WE	Working Electrode

Acknowledgements

First, I would like to express my deepest gratitude to my supervisor, Dr. Walter Mérida, for giving me the opportunity to be part of his research group. His guidance and continuous support throughout my M.A.Sc program is invaluable and much appreciated. Special thanks to Dr. Madjid Mohseni and Dr. Heather Trajano for serving on my thesis committee and taking the time to review my thesis.

I am indebted to two knowledgeable and helpful mentors and friends, Dr. Thomas Holm, and Dr. Jesus Diaz Real for their unconditional support, constructive advice and mentorship, especially during the tough times. This work would not be possible without their help.

Special thanks are owed to my family members in India especially my parents, Mr. Pawan Sharma and Mrs. Sudesh Kumari, as well as my grandparents who have supported me throughout my years of education.

I am also grateful to Dr. Beniamin Zahiri and Dr. Omar Herrera for offering valuable suggestions and guidance. I will cherish the great memories of working with Chun Haow Kung. Caroline Giacomini and Patrick Elsässer have also been quite helpful. Moreover, I would like to thank Guobin Sun from UBC Center for High-Throughput Phenogenomics (CHTP) for sharing his expertise on Micro-CT scanner and image analysis in Amira software. I also thank Mohamad Rezaei from 4D LABS for training me on laser micromachining tool. My appreciation extends to all my friends and colleagues at Rusty Hut and Clean Energy Research Centre (CERC) for their support whenever in need.

Lastly, I would also like to acknowledge the financial support from the University of British Columbia (UBC) and Mitacs Inc. in the form of awards.

1. Introduction

1.1 Research Background and Motivation

Porous carbon materials have many applications and have been applied to catalyst supports, electrochemical double layer capacitors, and fuel cells [1][2]. The characterization of porous materials is important in order to understand the overall performance of the materials [3]. For example, the porous structure influences the transport of gases [4].

The characterization of the porous structure of porous carbon electrodes is rather challenging due to the lack of precise characterization methods and detailed studies that correlates the size and shape of the particles with device performance. Gas adsorption methods such as BET (Brunauer–Emmett–Teller) method provide information about the total surface area, but do not allow the measurement of the pore size range of the electrodes [4,5]. In addition, by employing the nitrogen adsorption technique, it is difficult to detect pores larger than 0.1 μm [6]. Mercury intrusion porosimetry (MIP) is not suitable for soft materials since its operation at high pressure leads to deformation of pore structure, altering the electrode porosity [4,6]. The focused ion-beam scanning-electron microscopy such as used by Gunda et al. [7] to generate 3D microstructures of porous material with resolutions of nanometres is another characterization technique, however it's a destructive technique just like MIP. X-ray micro computed tomography (microCT) is an emerging and a non-destructive testing method [8]. It has been able to provide great insight into the 3D structure and heterogeneous porosity distribution of gas diffusion layers used in fuel cells [9–11]. However, it can also be time consuming, uneconomical and only allows for a representative sample measurement.

Electrochemical impedance spectroscopy (EIS) is a well-established analysis technique used to characterise the dynamic behaviour of electrochemical systems including porous carbon substrates

[2,12–17]. EIS is a non-destructive technique that has been successfully applied to study porous electrode/electrolyte interfaces [4,18]. Electrochemical impedance is the response of an electrochemical system to an applied ac potential. The frequency dependence of this impedance can help to identify the contributions from different components or processes to the total impedance of a porous electrode [19]. Impedance studies are of interest in several areas of electrochemistry including corrosion [20], electrocatalysis [21], photoelectrocatalysis [22], and nanostructured semiconductor electrodes [23,24]. Through fitting of the impedance spectra, more information about kinetic and electrode interfaces can be obtained than from alternative electrochemical methods, particularly by fitting data to equivalent electrical circuits [25]. The kinetics of double layer charging/discharging as a function of the pore size distribution (PSD) of the porous carbon electrodes has been studied by the researchers by employing EIS [26–28]. The advantage of EIS lies in the fact that it can potentially measure both total surface area (through overall capacitance measurements) [12,29] and contains information about the pore dimensions through the frequency dependence [6].

Although EIS is sensitive to porosity [30,31] and pore geometry [32–35], the pores in real porous materials are non-uniformly distributed having varying pore sizes and shapes [31,36] making analysis complicated. Often, an equivalent cylindrical pore structure is proposed to model the experimental impedance data yielding average values for the pore geometry. Thus, this approach does not provide accurate information about pore dimensions or shape. Preferably, a porous material could be characterized by the pore depth, pore diameter, the number of pores, the specific area, and the degree of uniformity of the porous structure [37].

This dissertation discusses the EIS measurements carried out on increasingly complex distribution of cylindrical pores with well-defined geometries made via drilling on graphite surfaces. The

complexity of the system was increased by stepping up from a single pore to multiple pores with uniform pore depth and radii followed by generating pore size distributions. The impedance response of the resulting porous electrodes was characterised with varying geometrical and electrochemical parameters - pore depth, pore radii, pore density (number of pores per unit area), and electrolyte conductivity.

1.2 Impedance of porous electrodes

1.2.1. Electric double layer

In an electrochemical system in which any electrode is immersed in an electrolyte, charge separation occurs at the electrode-electrolyte interface due to either an excess or deficiency of electrons at the electrode surface. In order for the interface to remain neutral, the charge held on the electrode is balanced by the redistribution of ions (from electrolyte) close to the electrode surface. This specific interfacial region is called the electric double layer [38,39]. Electric double layer capacitors (EDLCs), commonly known as supercapacitors store energy through the formation of an electrostatic double-layer of electronic and ionic charge accumulated on each side of the electrode/electrolyte interface [40,41]. The electrical properties of such a layer are important, since they significantly affect the electrochemical behaviour [38]. In an electrical circuit used to measure the current that flows at a particular working electrode, the double layer can be viewed as a capacitor. From the materials point of view, porous carbon materials have been commonly used as supercapacitor electrode materials [40,42].

1.2.2 Electrochemical Impedance Spectroscopy (The technique)

Impedance (Z) is the amount of resistance to the flow of current through an electronic component, circuit, or system, and it is measured in ohms (Ω). Impedance is measured by comparing the input signal, a voltage or current at a given frequency, to the corresponding output signal, which has passed through an electrical system that maintains its equilibrium or steady state. Repeating this measurement at a range of different frequencies provides a series called an impedance spectrum. Since this method is a frequency domain measurement technology, it is known as impedance spectroscopy (IS). When an electrochemical reaction (or so-called Faradaic process) is involved in the IS, the technique is referred to as Electrochemical impedance spectroscopy (EIS).

Impedance treatment is based on linear systems theory [43]. In general, the response of electrochemical systems is very nonlinear. Therefore, a small amplitude (~ 10 mV) AC sinusoidal perturbation, ($\Delta E = E_0 \exp(j\omega t)$) is applied on top of the controlled DC polarization potential so that the cell's response is pseudo-linear. In a linear (or pseudo-linear) system, the current response ($\Delta I = I_0 \exp[j(\omega t + \phi)]$) to a sinusoidal potential will be a sinusoid at the same frequency but shifted in phase. The ac impedance of the system is defined by Eq. (1) which is the ratio of Fourier transforms of the potential and current, and is equal to the ratio of the corresponding phasors [36]. Thus, the magnitude and phase shift depend on frequency.

$$Z(j\omega) = \frac{\Delta E}{\Delta I} = \frac{F(E(t))}{F(I(t))} = \frac{\tilde{E}}{\tilde{I}} \quad (1)$$

Two methods are most commonly used to represent impedance data graphically:

1. When the impedance values are drawn on a complex plane, i.e. the real values on x-axis ($\text{Re}(Z)$) and a negative imaginary values on the y-axis ($-\text{Im}(Z)$), the plot is called a Complex plane plot or Argand diagram, but commonly used in electrochemical literature by the

name of Nyquist plot. Each point on the plot represents the impedance value at a particular frequency.

2. Bode plots. There are two types of Bode plot:
 - (a) $\log |Z|$ (magnitude) versus $\log f$ (frequency)
 - (b) Phase angle ϕ versus $\log f$

The ac impedance measurements can either be performed in potentiostatic or galvanostatic mode. In potentiostatic mode the potential is controlled, where on the other hand in galvanostatic mode the current is controlled. In this work potentiostatic mode is applied.

1.2.3 Equivalent Electrical Circuit

EIS data is commonly analyzed by fitting it to an equivalent electrical circuit (EEC) model. Most of the circuit elements in the model are common electrical elements such as resistors, capacitors, and inductors. To be useful, the elements in the model should have a physical meaning in the physical electrochemistry of the system [44]. As an example, most models contain a resistor that models the cell's solution resistance.

Table 1.1 Impedance of Common Electrical Elements

Component	Current vs Voltage	Impedance
Resistor	$E = I R$	$Z = R$
Inductor	$E = L \, dI/dt$	$Z = j\omega L$
Capacitor	$I = C \, dE/dt$	$Z = 1/j\omega C$

Table 1.1 lists the common circuit elements, the equation for their current versus voltage relationship, and their impedance.

Impedance of a resistor is independent of frequency and has no imaginary component. The current through a resistor stays in phase with the voltage across the resistor. The impedance of an inductor increases as the frequency increases and vice-versa in case of a capacitor. Both inductor and capacitor have only an imaginary impedance component. The current through an inductor is phase-shifted -90° with respect to the voltage while the current through a capacitor is phase shifted 90° with respect to the voltage. From now on, the symbol L will be used only for pore depth.

When n linear impedance elements are in series, the equivalent impedance is given as:

$$Z_{\text{eq,series}} = Z_1 + Z_2 + \dots + Z_n \quad (2)$$

For a parallel combination of circuit elements, the equivalent impedance can be represented as:

$$\frac{1}{Z_{\text{eq,parallel}}} = \frac{1}{Z_1} + \frac{1}{Z_2} + \dots + \frac{1}{Z_n} \quad (3)$$

1.2.4 Impedance of cylindrical pores

An important reference point in the porous impedance studies is the work of De Levie [45,46] for cylindrical pores. De Levie developed a one-dimensional theory to calculate the impedance of electrodes consisting of cylindrical pores by the transmission line technique. This theory shows that the impedance spectrum of a porous electrode, with identical cylindrical non-connected pores having no faradaic reaction exhibits two features: a straight line with 45° slope at high frequencies

followed by a vertical capacitive straight line on the complex plane plot at low frequencies. This is shown graphically in Fig. 1.1 where arrow points the direction of increasing frequency. The assumptions of De Levie's model include cylindrical pore shape, electrolyte conductivity and interfacial impedance being independent of the location in a pore, and no curvature of the equipotential surface in a pore. The last assumption is not applicable to a rough surface with shallow pores.

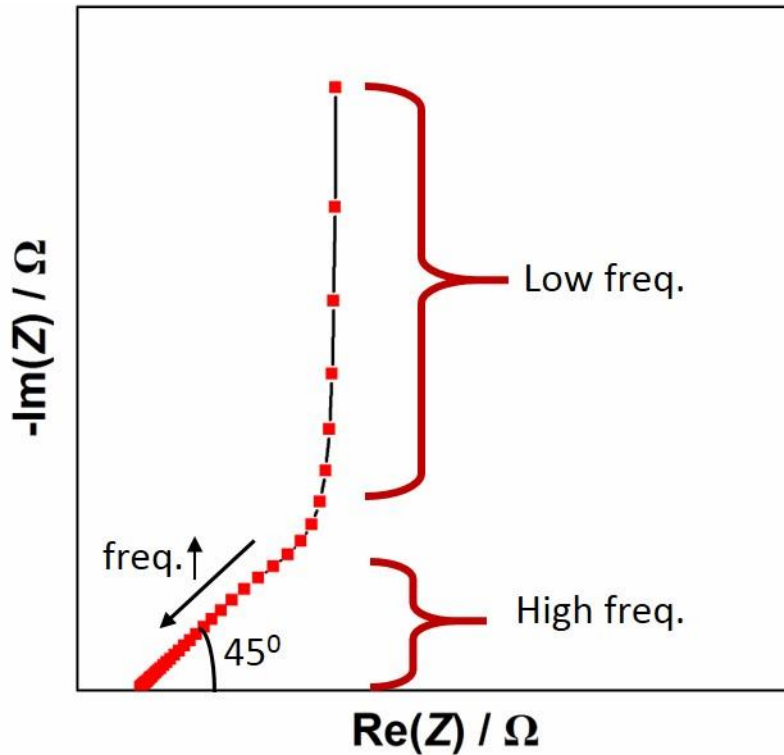


Fig. 1.1 Typical Nyquist plot for an ideal porous electrode

The total impedance of a porous electrode in the absence of DC current can be described as [45] :

$$Z_t = R_{sol} + Z_{pore} = R_{sol} + \frac{R_{\Omega,p} \lambda}{L} \coth\left(\frac{L(j)^{1/2}}{\lambda}\right) \quad (4)$$

where

$$R_{\Omega,p} = \frac{\rho L}{n\pi r^2} \quad (5)$$

$$\lambda = \left(\frac{r}{2C_{dl}\omega\rho} \right)^{1/2} \quad (6)$$

R_{sol} is the solution resistance of the electrolyte outside the pores, r and L are the radius and length of a pore, ρ the resistivity of the electrolyte, $R_{\Omega,p}$ the electrolyte resistance in the pore, n is the number of pores, and C_{dl} refers to the specific double layer capacitance. The penetration depth denoted by λ is a quantity characterising the fraction of the pore effectively involved in the ac measurements [46]. It is a significant indicator when trying to understand the charging and discharging process for electric double layer capacitors (EDLCs) in porous carbon electrodes [17,28].

1.2.5 Transmission Line Equivalent Circuit Model

The porous capacitive electrodes cannot be represented by a simple connection of the resistor, capacitor, or inductor elements. It can be represented only by a semi-infinite series of distributed R-C(resistor-capacitor) elements called transmission line [36,45,47], as represented in Fig. 1.2. This representation is equivalent to Eq. (4) given by De Levie. This type of distributed characteristic exists even when all system properties are homogeneous and space-invariant [6]. Some authors [28,48] tried to use the transmission line circuit to approximate experimental data using a sufficient number of RC elements and verifying whether the number of these parameters was sufficient. This procedure can approximate experimental impedances and is more tedious, but

the use of Eq. (4) is more appropriate as it allows for the direct estimation of certain parameters and their standard deviations.

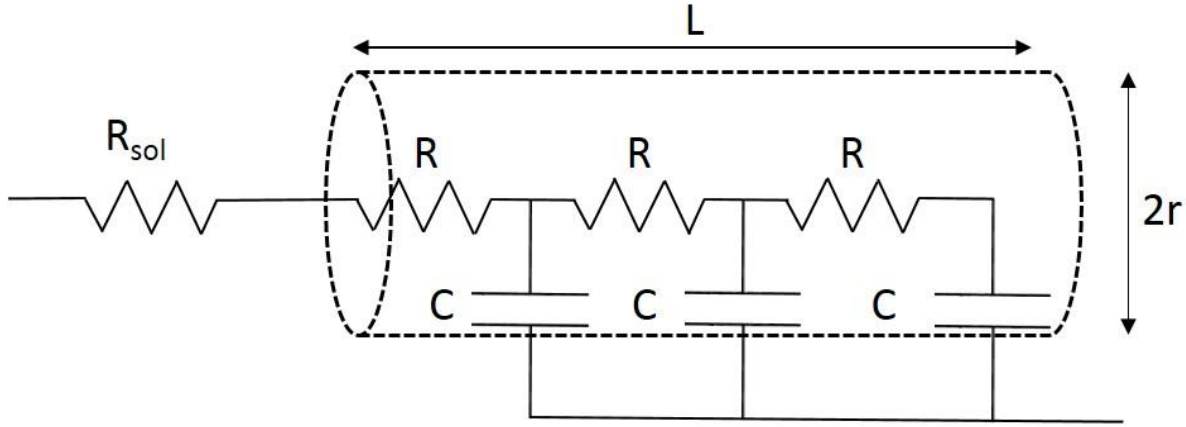


Fig. 1.2 Distributed Resistance and Capacitance in a Pore Represented by the Transmission Line Model

1.2.6 Influence of Pore Geometry on Impedance

In practice, the pore geometry influences the impedance spectra. The effect of pore geometry was first modelled in detail by Keiser et al. [32], following on closely from the work of De Levie [45], where a pseudo-3D numerical model was used to generate impedance spectra for a range of close pore geometries. They reported that the impedance curve in the Nyquist plot changes with the shape of a pore in the intermediate frequency region while being similar to that of a cylindrical pore at extremely low or high frequencies. Elout et al. [33,34] developed the matrix method to calculate the impedance of a non-cylindrical pore by extending Keiser's model. They drilled pores into stainless steel surfaces and found that the one-dimensionality condition is satisfied for length/radius ratio larger than two. The current distribution over the pore section becomes non-uniform for smaller ratios resulting in smaller virtual pore radii (compared to the real pore dimensions). This aspect makes the porous surfaces differ from rough surfaces as for porous

electrodes the length/radius ratio is important. In addition, a few articles by Lasia and his co-workers [31,36,49] stressed the contribution of flat part of porous electrodes should be added to the isolated pores impedance. They also showed its effect on the shape of impedance spectra at high frequencies by comparing different ratios of flat part to porous part capacitances.

1.2.7 Impedance Spectroscopy for Porosimetry Studies

Electrochemical impedance spectroscopy (EIS) has been applied to characterize carbon electrodes in other studies and has been found to be a useful tool in the design and characterization of these electrodes [15,50–52]. Candy et al. [29] reported the impedance of gold-powder and Raney gold and found that the overall impedance could be represented by an equivalent cylindrical pore electrode with average values of pore radii, pore depth and the number of pores. In the case of pore radii distribution, this problem was treated by Song et al. [6,53] and demonstrated by successfully fitting experimental impedance data for a gold powder electrode [29] and a carbon membrane [12]. A recent study by Cericola and Spahr in 2016 [4] analysed the effect of particle size, shape and orientation on the performance of graphite electrodes and found that material particle shape strongly affected the pore resistance.

1.3 Significance

Most of the works discussed in the section 1.2 try to probe real porous materials directly through De Levie's TLM formula for impedance and propose an equivalent cylindrical pore structure, i.e., equivalent pore radii, pore depth and number of pores. However, this approach does not provide reliable information about pore dimensions or shape as it only provides averages for the pore parameters. More complex distributions of pore parameters (pore radii or pore depth) make it

difficult to confirm the applicability of the TLM experimentally. In this work, a simple and systematic approach is adopted to understand the distributed pore impedance by creating scaled up cylindrical pores with known pore dimensions obtained via Computerized Numerical Control (CNC) drilling. The pore structure complexity was gradually increased starting with the evaluation of single pore impedances followed by drilling multiple pores with uniform pore dimensions and finally generating pore size distributions (PSD) having distributed pore radii or depth or a combination of both. The approach demonstrated in this work allows for the comparison between the experimental and theoretically predicted impedances without assumptions about electrode structure (the pore dimensions and number of pores are well-defined.) The effect of geometrical and electrochemical parameters, i.e., pore depth, pore radii, number of pores, and electrolyte conductivity are investigated in detail.

1.4 Objectives

There are two main objectives of this work. The first aim is to demonstrate an experimental framework to verify the pore impedance for increasingly complex geometric systems based on modified De Levie's transmission line model by a systematic approach yielding physically meaningful parameters. The second is to correlate graphite electrode geometrical parameters – pore depth, pore radii, and pore density and electronic parameters – electrolyte conductivity, with the impedance response of the electrode by decoupling each parameter and studying them one at a time.

1.5 Thesis Layout

This thesis compiles the results achieved throughout the course of this research, and discusses them in the form of two chapters following introduction and experimental methods chapters. The objectives of this research were achieved through a series of well controlled experimental work carried out at the University of British Columbia (UBC).

The information gathered is presented as follows:

Chapter 1: Presents a general background on the research topic. Provides a comprehensive literature review about the impedance of porous electrodes. Research objectives are articulated and the significance of this research is addressed in this chapter. The layout illustrating the thesis organization is also discussed in this chapter.

Chapter 2: Provides detailed description of the experimental plan and research methodology as well as all the assays and analytical techniques employed in this study.

Chapter 3: Provides the results obtained by carrying out electrochemistry on the pores created on graphite, glassy carbon electrodes along with the surface characterization results. The impedance results for single pore, ordered uniform pore arrays were analyzed using ZView fitting and a graphical approach in order to verify porous impedance and get physically meaningful parameters. The pore geometry and conductivity of electrolytes were varied in order to verify the theoretically predicted outcomes of their variations on the impedance response of the porous structure.

Chapter 4: Presents overall conclusions, summarizes the key findings of the work, and provides recommendations for future research.

2. Experimental Systems and Experimental Methods

In order to achieve the desired objectives of this research, electrochemistry was initially performed on pores made on Glassy carbon discs followed by performing electrochemical measurements on pore structure created on graphite samples. The detailed methodology of sample preparation and electrochemical results obtained are discussed in this and the following chapter. It is worth mentioning here that results for the former were not so promising, after which all the experiments were performed on pore arrays created using graphite as a substrate. Hence, most of the discussion is centred on the graphite electrodes in this work.

2.1 Sample Preparation

2.1.1 Preparation of Glassy Carbon Samples

Glassy carbon (GC) disc with 10 mm diameter, 2 mm thickness (Sigradur G from HTW Hochtemperatur-Werkstoffe GmbH) was used as substrate initially. Prior to any treatments, the bare GC disc was polished to a mirror finish with 1 μm monocrystalline diamond suspension (Allied High Tech Products Inc.) on a polishing cloth. The polished GCs were successively cleaned with acetone, isopropyl alcohol, and deionized (DI) water for 20 min each in an ultrasonic bath. The GC sample surface was covered with Kapton tape (CHR® Polyimide Adhesive tape, Saint-Gobain) leaving an area of 1 mm \times 1 mm uncovered at the centre of the GC disc. An attempt was made to create an ordered, uniform pore array (11 \times 11 pores) consisting of cylindrical pores with pore diameter = 45 μm , pore depth = 400 μm on this GC sample by employing laser micromachining workstation (IPG Photonics, IX-280-ML) in the exposed area. The Solidworks

design of the pore array was exported to IPG's Chroma.NET software which performed the required laser process.

2.1.2 Preparation of Graphite Samples

For the graphite samples, an isostatically pressed Graphite plate (Grade GM-10) obtained from Graphitek™ LLC was used. Firstly, for each experiment graphite piece (2.1 cm × 2.1 cm × 7.2 mm), a fine finish was obtained with the help of Roland MDX-40A High Precision CNC (Computer Numerical Control) Milling Machine. The bare graphite piece was first cleaned with acetone followed by isopropyl alcohol and milli-Q water (resistivity 18.2 MΩ cm) to remove any organic contaminants. The top surface of graphite (2.1 cm × 2.1 cm cross-section) was covered with the Kapton tape (CHR® Polyimide Adhesive tape, Saint-Gobain). The desired cylindrical pores were then created in the direction perpendicular to the top surface using different sizes of 'Wire Gauge Size Quick-Change Carbide Drill Bits' (diameters of 0.46 mm, 0.66 mm, 0.74 mm, 1.02 mm, 1.32 mm) supplied by McMaster-Carr using the CNC milling machine. Thus, the Kapton tape surrounding the top surface area around the pores ensured that only the pore wall area (drilled pore area) was exposed to the electrolyte while performing the experiments.

2.2 Experimental Setup

All the measurements reported in this work were done using a three-electrode cell made with the help of Acrylic sheets (McMaster-Carr) (shown in Fig. 2.1). In a three-electrode setup, the working electrode (WE) is the electrode whose interface is under investigation. The potential of the WE is monitored relative to a separate reference electrode (RE). The counter electrode (CE) is used for

measurement of the current flowing through the cell. It is usually chosen to be an electrode that does not produce substances by electrolysis that will reach the working electrode surface and cause interfering reactions there [54]. The graphite piece with the drilled pores surrounded by the Kapton

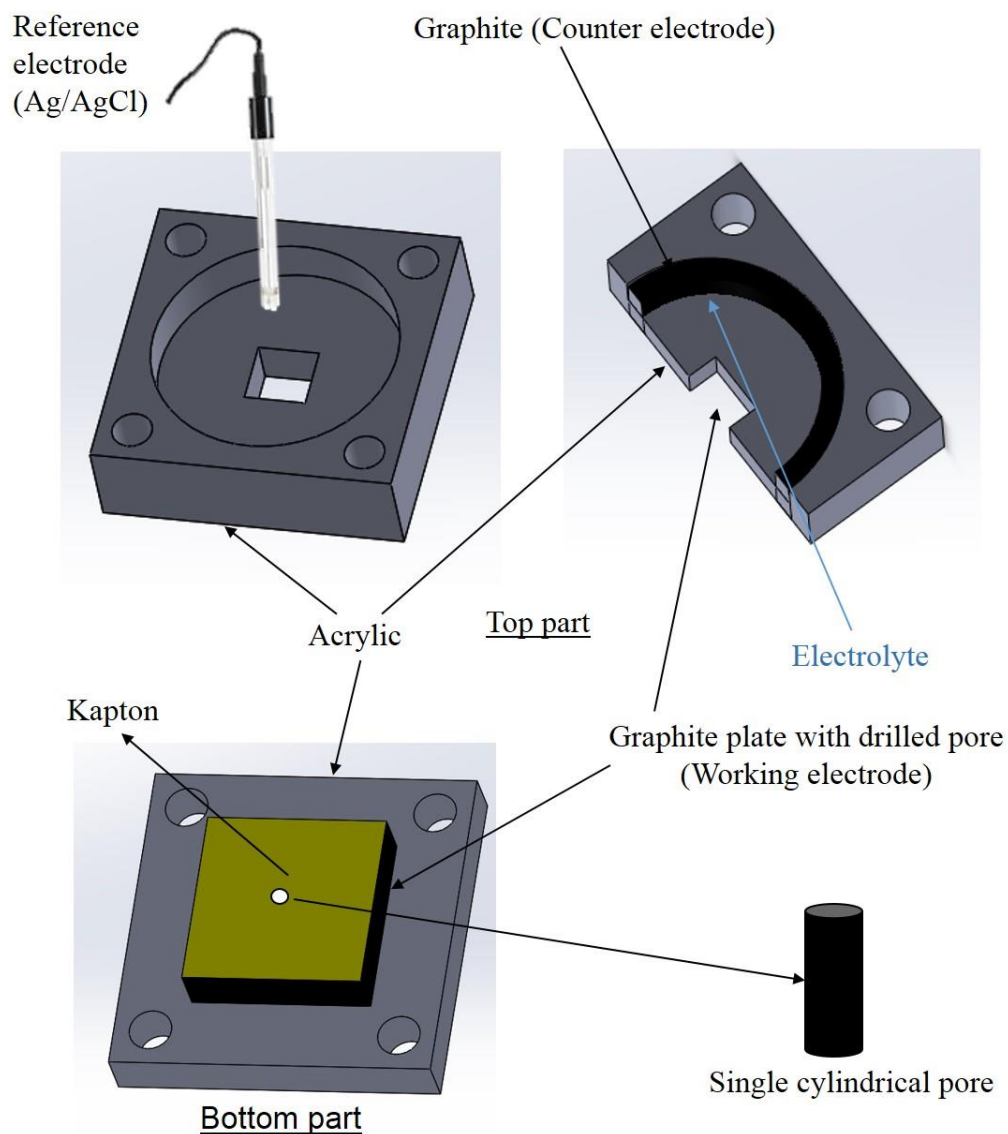


Fig. 2.1 Sketch of Experimental Setup

tape was fixed to an acrylic piece (3.9 cm × 3.9 cm × 6 mm) at the bottom with the help of 3M™ 9087 High Performance Double Coated Tape. This graphite sample connected to a copper current collector served as the WE. The dimensions of the acrylic sheet used for the top portion of the setup (shown in Fig. 2.1) were 3.9 cm × 3.9 cm × 1.8 cm. Graphite rod (Graphtek™ LLC) served as the CE and a commercial Ag/AgCl (3.8 M KCl) electrode (Pine Research) was used as the RE. The distance between the RE tip and the WE was kept fairly constant (1-2 mm). The area of the CE is much larger (~12.8 cm²) than the area of WE to ensure kinetics of the reaction occurring at CE do not interfere with the measurement at the WE. The air bubbles in the pores were removed by poking pores gently with a graphite pencil leads (Pentel) having a radius slightly smaller than the pore radius. The electrolytes used for the experiment consisted of 1.0 M H₂SO₄, 0.1 M H₂SO₄ solutions prepared from concentrated sulphuric acid (reagent grade, 95% purity, Sigma Aldrich), 1.0 M HClO₄, 0.1 M HClO₄ solutions prepared from concentrated perchloric acid (70% purity, Veritas® Double Distilled, GFS chemicals), 1.0 M NaOH and 5.0 M NaOH solutions prepared from sodium hydroxide pellets (ACS reagent, 97% purity, Sigma Aldrich). Milli-Q water (resistivity 18.2 MΩ cm) was used for preparation of all the solutions. A similar setup was used for electrochemical measurements done on pores created via laser micromachining on glassy carbon substrate with the GC sample being connected to a copper current collector serving as the WE, and using the same RE, CE as were used in the case of graphite. The electrolytes used in the case of GC pores were 0.5 M H₂SO₄ solution, 0.5 M HClO₄ solution.

2.3 Electrochemical Characterization

Electrochemical measurements were performed for the graphite samples using a BioLogic VMP3 potentiostat and for the GC samples using a Biologic SP-150 potentiostat. A potentiostat is used

to accurately control the potential of the interface under investigation (working electrode) and to accurately measure the current flowing to the working electrode (WE). In both the cases, measurements were carried out at room temperature ($20 \pm 2^\circ\text{C}$). For each sample, the open circuit potential (OCP) was recorded for 15 min to allow steady conditions to be reached. Cyclic Voltammograms (CV) were first run in a potential window of 0.3 to 0.5 V vs Ag/AgCl Ref for acids and -0.2 to 0.0 V vs Ag/AgCl Ref for bases at a scan rate of 50 mV/s and 50 cycles to confirm that the electrode surfaces were kept clean and were stable over several cycles. Electrochemical impedance spectroscopy (EIS) measurements were then carried out in the frequency range from 100 kHz to 100 mHz by applying a sinusoidal perturbation signal of 10 mV_{rms} amplitude, at a potential of 0.4 V vs Ag/AgCl in case of acidic and -0.1 V vs Ag/AgCl in case of alkaline solutions. The sampling frequency was such that the measurements points were equally spaced in a logarithmic scale taking 10 points per decade. The potential for EIS measurements was chosen to avoid faradaic reactions as was evident by the quasi-rectangular shapes of Cyclic Voltammograms (CVs) in the potential window measured. At this potential, the impedance response has contributions only from ohmic resistance, the distributed resistance of electrolyte inside pores, and electric double layer capacitance. Thus, the EIS response can be understood in terms of these processes. The CV, EIS measurements were done at time $t = 0$ and $t = 1$ hour for the graphite samples and compared to check their repeatability and stability of the sample. The measurements for $t = 0$ and $t = 1$ hour were compared to check whether they were similar (fitted parameters standard deviation $< 10\%$) else measurements were performed on a new set of drilled pores. The GC samples had to stay in the electrolyte for a longer time, around 4 hours to see the quasi-rectangular shape of CV, or in other words nearly complete electrolyte percolation to the bottom of the pores. The plot of CVs obtained for various cases are shown later in chapter 3.

The experimental framework for the proposed work (for graphite electrodes) is summarised in Table 2.1 while Fig. 2.2 shows the schematic of the experimental framework. Although the pores investigated in this work are of micrometer size (pore radii $\geq 230 \mu\text{m}$), the obtained results for the pore radii and pore depth variation on the impedance response should be similar for smaller pores as long as the ion migration is not restricted by the pore radii ($< 10 \text{ nm}$). [55]

Table 2.1 Summary of the experimental framework

Experiment	Pore Dimensions					
	Pore Diameter (mm)		Pore Depth (mm)			
Single pore (Verify electrolyte choice) (0.1 M HClO ₄ , 1.0 M HClO ₄) (0.1 M H ₂ SO ₄ , 1.0 M H ₂ SO ₄) (1.0 M NaOH, 5.0 M NaOH)	1.00		3.00			
Single pore: same pore radii, different pore depths (1.0 M H ₂ SO ₄)	0.74		3.00	3.80	5.20	6.60
Single pore: same pore depth, different pore radii (1.0 M H ₂ SO ₄)	0.46	0.66	1.02	1.32	5.20	
Multiple pores: Uniform pore array (1.0 M H ₂ SO ₄) : 1 pore, 4 pores, 8 pores	0.74		3.70			
Multiple pores: Non-Uniform pore array (1.0 M H ₂ SO ₄)	a) Vary pore radii b) Vary pore depth c) Vary pore radii + pore depth					

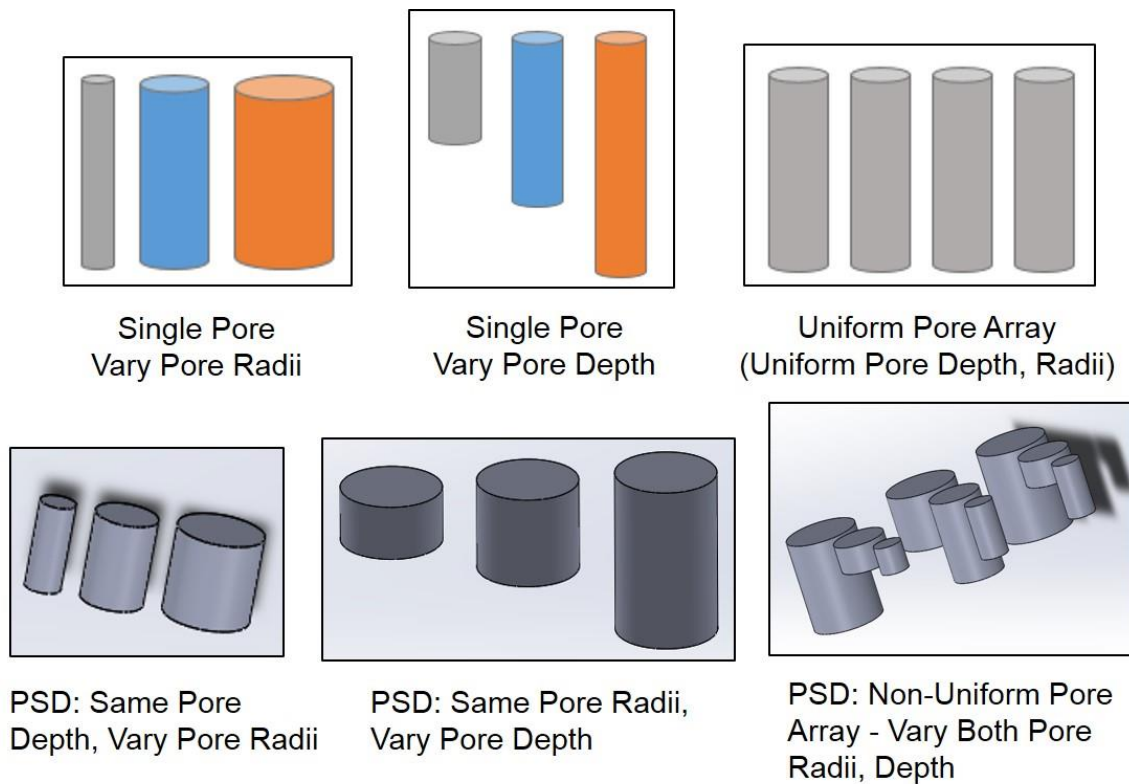


Fig. 2.2 Schematic of Experimental Framework

2.4 Surface Characterization

The surface characterization of the samples (both glassy carbon and graphite) was done by employing X-ray micro computed tomographic (Micro-CT) microscopy. A Micro-CT specimen scanner (Scanco Medical μ CT 100) was used to obtain high-resolution 3D reconstruction of the pores. The resolution of the Micro-CT scanner used was 10 μ m per voxel side (for each of the X, Y, Z axis) for the graphite samples which was good enough for the pore sizes considered in this work. In the case of GC samples, resolution of the Micro-CT scanner used was 7.4 μ m per voxel side. The Micro-CT scan images were analyzed using the Amira Software for FEI Systems 6.0.1 (Thermo Fisher Scientific) to obtain the pore dimensions and confirm the pore shape for the

cylindrical pores drilled. This imaging software also allowed to obtain 2D images in the through-plane direction (cross-section parallel to the direction of pores drilled) to verify the pore dimensions.

2.5 EIS Data Interpretation

Two methods were used to extract the distributed resistance and capacitance values from the impedance data, ZView fitting and a graphical method. Notably, the electrodes did not exhibit ideal capacitive behavior. This is expected and the electric double layer (EDLCs) show frequency-dependent capacitance even though it should ideally be independent of frequency.[17,53,56] Experimental impedance plots of porous electrodes do not necessarily exhibit perfect 45° slope at high frequencies and 90° phase angle at low frequencies compared to the ideal case discussed by De Levie, and this was indeed the case in this study. Following this, constant phase elements (CPEs) are commonly used to fit impedance data to compensate for the ideality [31,36,57] and the impedance of a CPE is given by Eq. (7)

$$Z_{\text{CPE}} = \frac{1}{Q(j\omega)^\alpha} \quad (7)$$

Here Q is the CPE parameter, α is the CPE coefficient, ω is the angular frequency. Notably, if $\alpha = 1$, the CPE element is equal to an ideal capacitor.

2.5.1 ZView Fitting (1st approach)

This approach consists of a fitting procedure based on Complex Nonlinear Least-Squares Analysis technique in ZView software (Version 2.90, Scribner Associates) that allows the fitting of

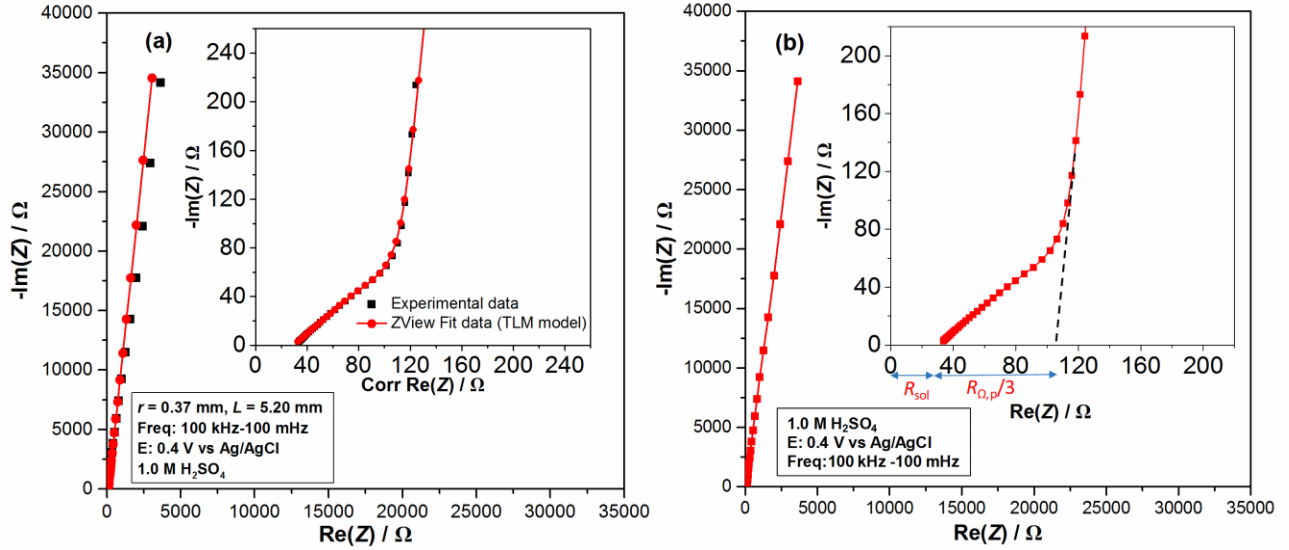


Fig. 2.3 (a) Example of fitting impedance data with ZView for a single pore, inset-high frequency data **(b)** Determination of $R_{\Omega,p}$ value by the graphical method for pore diameter = 0.74 mm, pore depth = 5.20 mm

impedance data by constructing an appropriate model. Essentially, ZView has an inbuilt DX Type 12-Bisquert #3 element[58,59] that allows us to obtain fitted resistance and CPE parameter Q value per unit depth, the CPE coefficient α to characterise inhomogeneity wherein values of pore depth and solution resistance R_{sol} are fixed. The former is already known and the latter determined graphically from the experiment by measuring the intercept on real axis by extrapolating the high frequency data. In this model, the contribution of the bottom part of the pores to the impedance is neglected since for the chosen pore sizes, the pore with smallest aspect ratio (L/D) has a ratio of curved to bottom part area ~ 16 which accounts for 6.25% of the total pore area. All other pores with higher aspect ratios account for less than 5% of the total pore area in the area normalised calculations of electrochemical parameters.

Since Q has the unit $\mu\text{F cm}^{-2} \text{s}^{\alpha-1}$, it is hard to compare the results for different α values. Therefore the Brug's formulae[60] was used to calculate the equivalent capacitance with the approach suggested by R. Jurczakowski et al.[31] using the sum of R_{sol} and $R_{\Omega,\text{p}}$. The Brug's formulae in this form is presented in Eq. (8).

$$C_{\text{dl}} = Q^{\frac{1}{\alpha}} \left(R_{\text{sol}} + \frac{R_{\Omega,\text{p}}}{3} \right)^{1-\alpha/\alpha} \quad (8)$$

Note that while evaluating C_{dl} by the Eq. (8), Q and $R_{\Omega,\text{p}}$ are expressed in absolute values and then absolute capacitance normalized by pore wall area to give C_{dl} values. An example of the ZView fitting procedure is demonstrated in Fig. 2.3(a).

2.5.2 Graphical Method (2nd approach)

In this method, both the $R_{\Omega,\text{p}}$ and Q values are obtained by using a graphical approach. The plot of the logarithm of the imaginary part of the impedance vs. the logarithm of frequency is fitted by a straight line for a frequency range one order of magnitude lower than the transition frequency (transition frequency same as the breakpoint frequency defined in R. Jurczakowski et al.[31]) where the plot is sufficiently linear and gives us the CPE coefficient α . This is based on the graphical approach suggested by Orazem et al. [61]. The transition frequency is defined as the frequency below which the EIS response begins to exhibit capacitive behaviour, with a nearly straight line parallel to the imaginary impedance axis in a Nyquist (Complex) plot [62,63]. An example is shown in Fig. 2.4(a) with calculated data and the best fitted straight line. Fig. 2.4(b) shows the value of Q calculated using Eq. (9) given by Orazem et al. [61] at various experimental frequencies, the frequency range being the same as used for finding α .

$$Q = \sin\left(\frac{\alpha\pi}{2}\right) \frac{1}{(-\text{Im}(Z))\omega^\alpha} \quad (9)$$

These values are all within 2.6 % of its average value, which is shown as a stippled line in Fig. 2.4(b) at $389.64 \mu\text{F cm}^{-2} \text{s}^{-0.052}$. In order to calculate effective capacitance from CPE parameters,

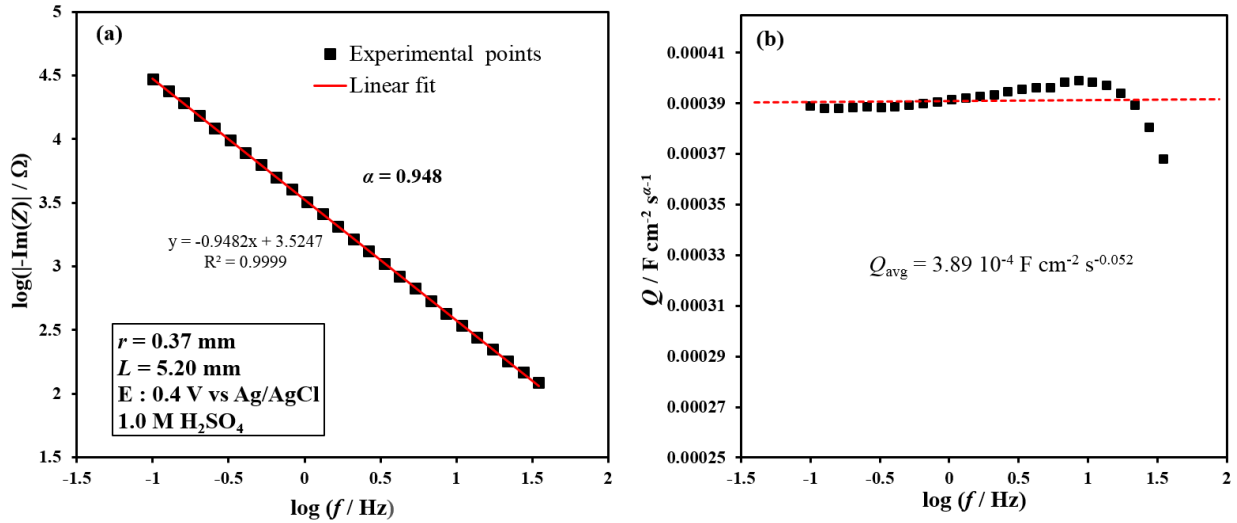


Fig. 2.4 Analysis of experimental data by graphical method (a) imaginary part of impedance vs frequency plot (b) frequency dependence of CPE parameter Q

Eq. (8) was used, as was the case in the 1st approach. Similarly, to calculate $R_{\Omega,p}$, the low frequency portion of the impedance data at frequencies an order of magnitude lower than the transition frequency was extrapolated down to the real axis and the corresponding intercept on the real axis equals $R_{\text{sol}} + R_{\Omega,p}/3$ [64,65]. Since R_{sol} is known from the high frequency experimental data as explained earlier in the 1st approach, $R_{\Omega,p}$ can be evaluated. This approach is illustrated in Fig. 2.3(b).

3.1 Results

3.1 Initial Trials on Glassy Carbon Samples

In this section, the impedance studies done on an exposed top geometrical area of 1.21 mm^2 of the GC sample consisting of the 11×11 cylindrical pore array ($r = 22.5 \text{ }\mu\text{m}$, $L = 400 \text{ }\mu\text{m}$) and flat part of the GC are discussed. Fig. 3.1 shows the Nyquist plot obtained experimentally using 0.5 M

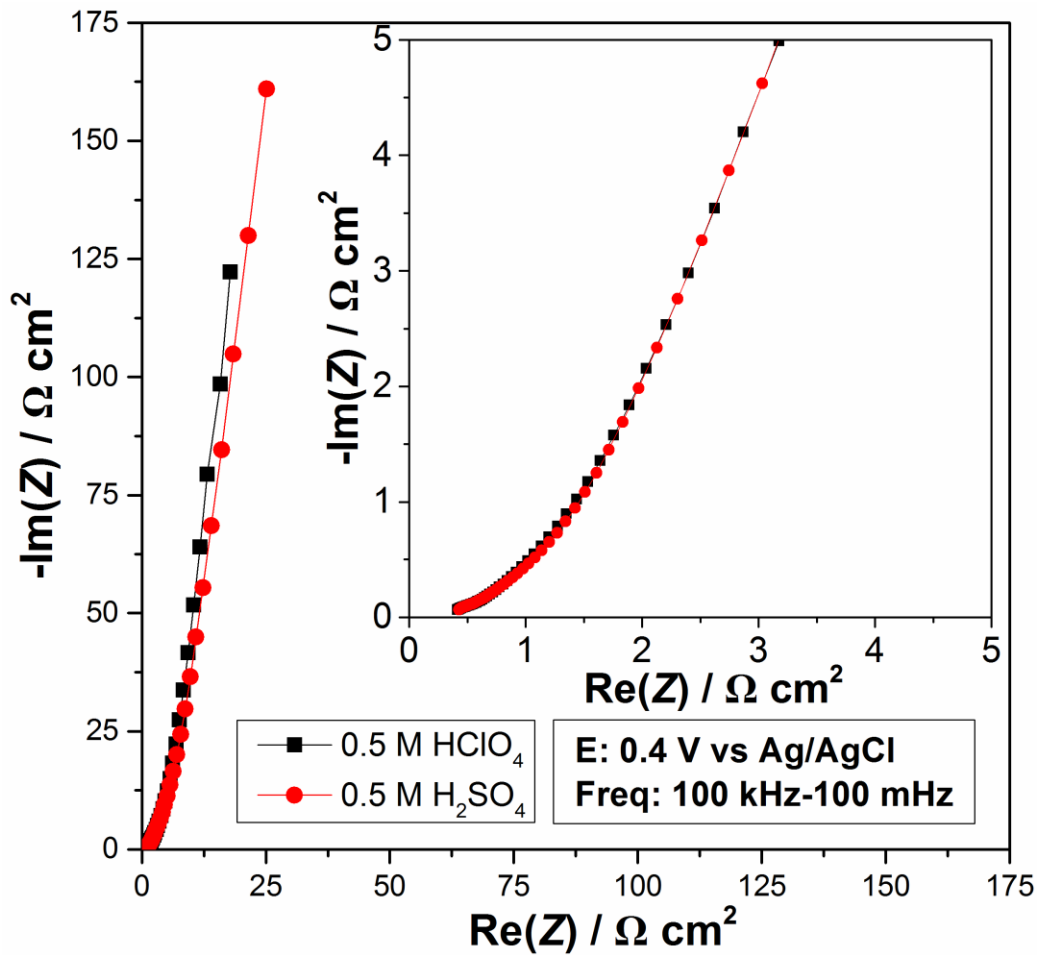


Fig. 3.1 Nyquist plots for experimental data of 11×11 pore array ($r = 22.5 \text{ }\mu\text{m}$, $L = 400 \text{ }\mu\text{m}$) in $1.1 \text{ mm} \times 1.1 \text{ mm}$ area of Glassy carbon sample for two different electrolytes

H₂SO₄ and 0.5 M HClO₄ solutions. The corresponding Nyquist plots looked quite similar when compared at the high frequencies with a slight shift in the low frequency region. This was as expected since the conductivities of 0.5 M H₂SO₄ and 0.5 M HClO₄ are not too different ($K = 0.396 \Omega^{-1}\text{cm}^{-1}$ and $K = 0.358 \Omega^{-1}\text{cm}^{-1}$ respectively). Hence, the impedance response should be similar for the same porous morphology and flat part area. However, the shape of the Nyquist

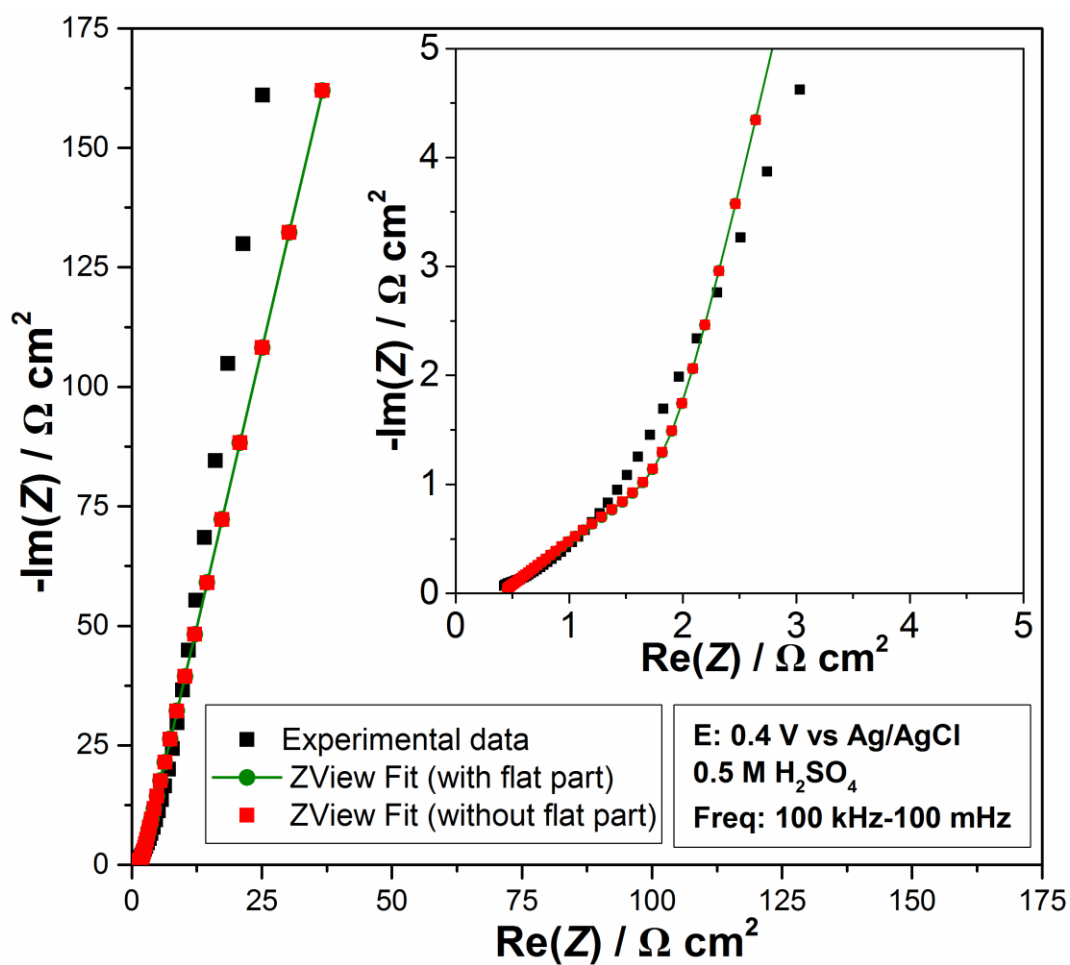


Fig. 3.2 Nyquist plots for experimental data and ZView fitted plots of 11×11 pore array ($r = 22.5 \mu\text{m}$, $L = 400 \mu\text{m}$) in $1.1 \text{ mm} \times 1.1 \text{ mm}$ area of Glassy carbon sample

plot deviated from the expected behaviour seen for a typical cylindrical pore arrangement. This was illustrated through the ZView fitting results shown in Fig. 3.2, which were obtained in two ways: considering flat part contribution to the impedance and ignoring its contribution in the other case. In the former case, the capacitance of flat part (considering the CPE behaviour) Q_{flat} was added in parallel to the porous impedance as shown in Fig. 3.3 where Z_{pore} is same as given by

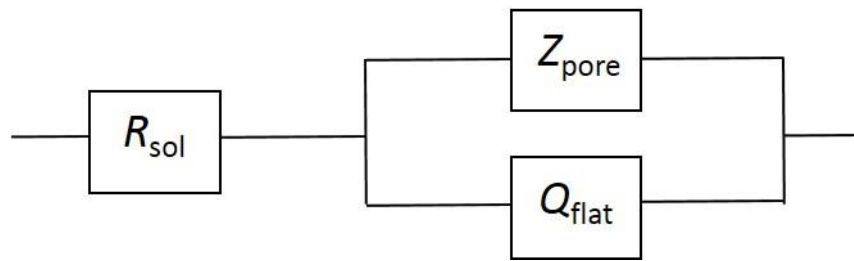


Fig. 3.3 Equivalent circuit used to fit impedance of 11×11 pore array in $1.1 \text{ mm} \times 1.1 \text{ mm}$ area of Glassy carbon sample

Eq. (4) with the CPE parameters included. In the latter case, the equivalent circuit used was the same as shown in Fig. 1.2 with the incorporation of CPE. The fitting curves with and without the flat part in Fig. 3.2 show similar results, at least at low frequencies, indicating that the flat part capacitance contribution to the total impedance is minimal. The GC drilled pores showed discrepancy from ideal behavior, therefore, the pores were imaged using Micro-CT scanning, and the results are shown in Fig. 3.4. These images show that the pore cross section becomes narrower after a certain depth and does not remain cylindrical throughout from the pore orifice to the bottom. In addition, the pore volume of a single pore was obtained by summing up the individual contributions of segmented slices (at various cross-sections) by using image analysis tools in

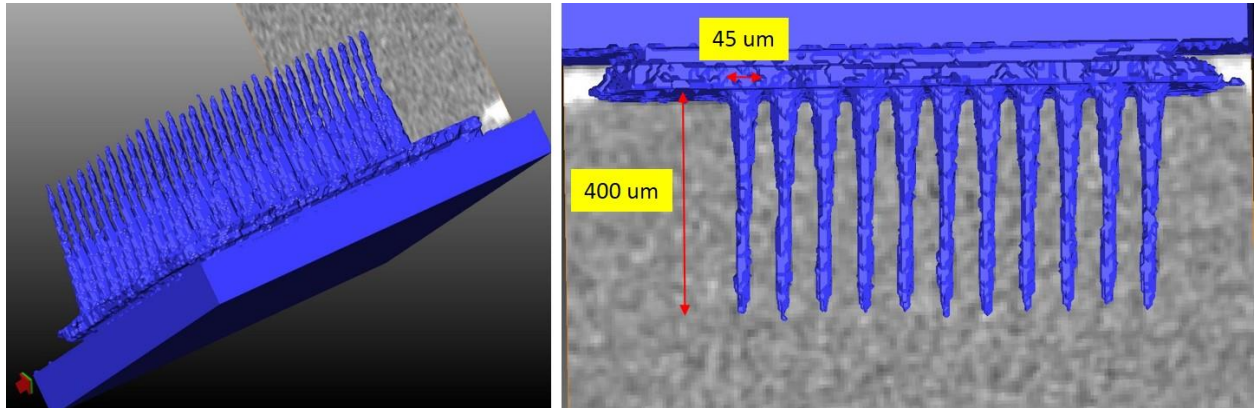


Fig. 3.4 Micro-CT scan images of 11×11 pore array in $1.1 \text{ mm} \times 1.1 \text{ mm}$ area of Glassy carbon sample (Resolution $7.4 \text{ }\mu\text{m}$ / voxel side)

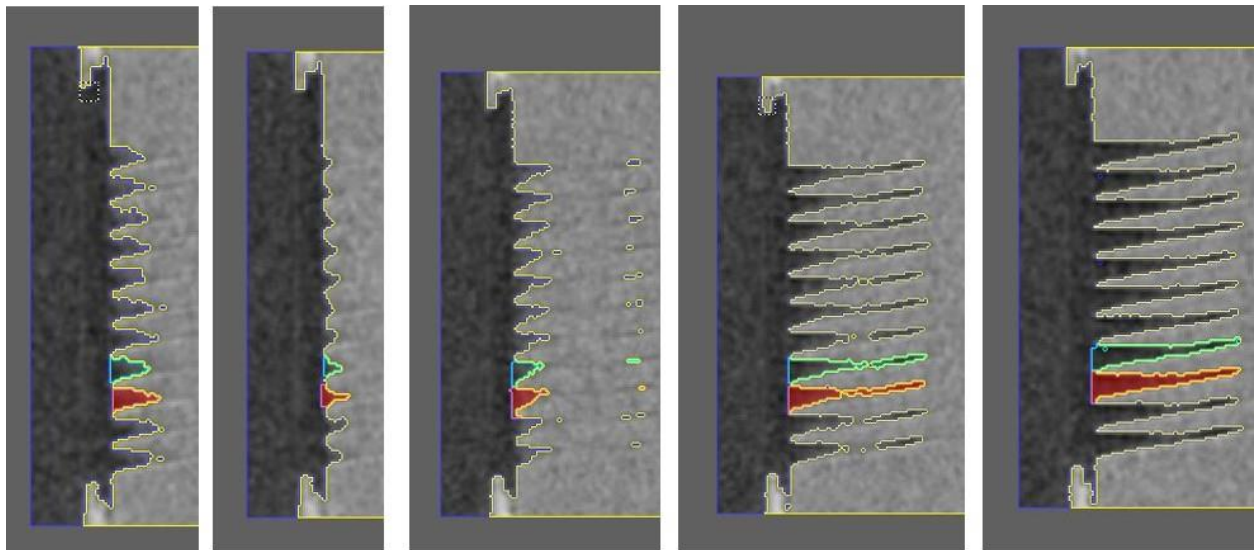


Fig. 3.5 Segmented slices of the pores created by laser micromachining on Glassy carbon sample

Amira software as shown in Fig 3.5. The analysis showed that the volume enclosed by a pore was around 75.79 % of that of a cylindrical pore ($\pi r^2 L$) with perfect shape. Hence, the effect of pore

geometry could explain the lack of good fit obtained by using TLM model based on cylindrical pore shape. Thus, the laser micromachining technique did not give satisfactory results for a uniform pore array due to its inability to create idealized cylindrical pore shape. Since further experiments were supposed to be conducted on non-uniform pore arrays based on the former's impedance response, it was decided not to use this technique any longer and all the subsequent experiments were performed with the drilling technique. In addition, the GC disc being used was only 2 mm thick so graphite plate substrate was alternatively chosen to create deep enough pores. The results obtained through the latter method are discussed in details in the following sections of this chapter.

3.2 Verification of Pore Geometry (Graphite Samples)

The pore dimensions and shape of the cylindrical pores drilled on graphite pieces were confirmed by using Micro-CT scan technique. Fig. 3.6(a) shows the 2D images for varying pore depths for a single pore with same diameter ($D = 0.74$ mm) in the through-plane direction of the drilled cylindrical pores. Fig. 3.6(b) shows the 2D images for the case of varying pore radii for a single pore having the same pore depth ($L = 5.20$ mm) with the pore dimensions specified in respective figures. The 3D images of the pores for the case shown in Fig 3.6(a) are illustrated in Fig. 3.6(c-d). From Fig. 3.6, it is evident that the drilled pores are cylindrical with a slight offset at the pore bottom due to point angle of 135° .

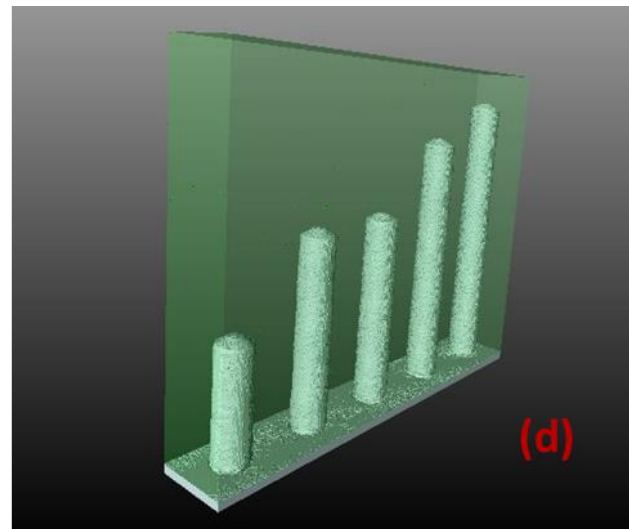
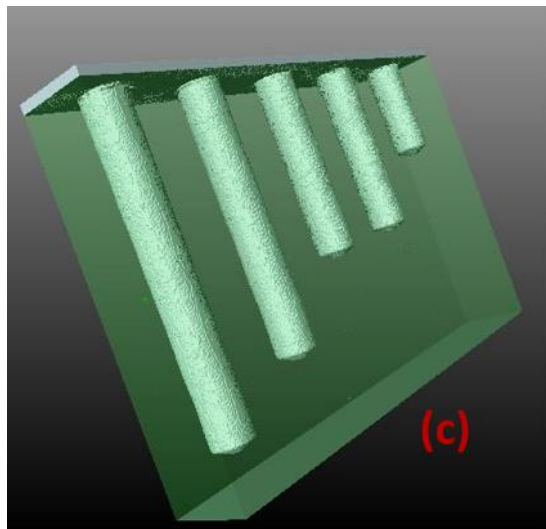
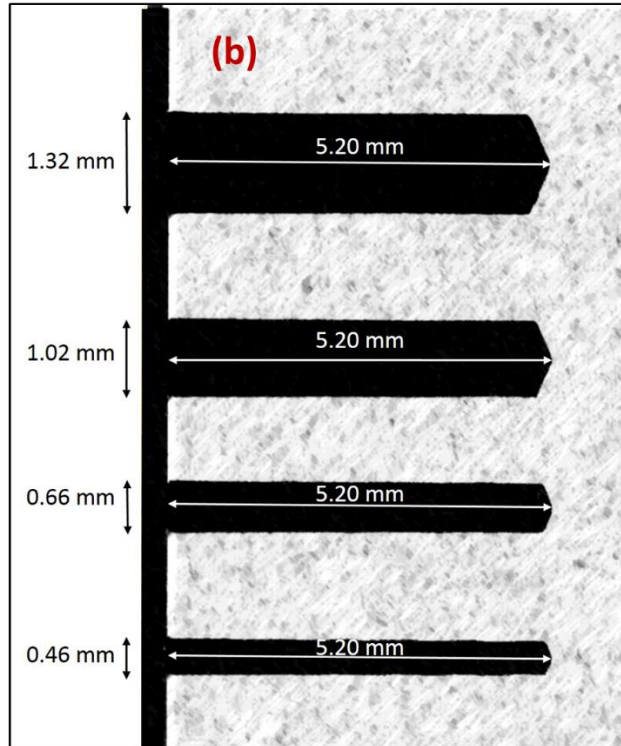
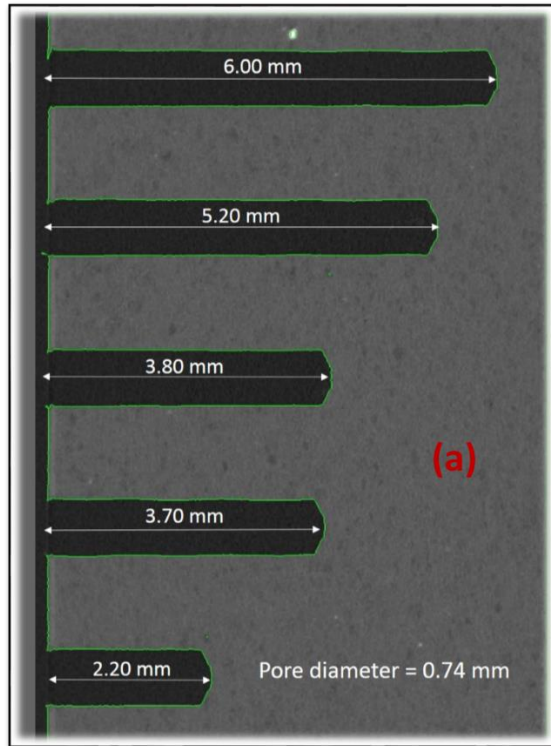


Fig. 3.6 Micro-CT scan images of cylindrical pores drilled on graphite piece (a) 2D image of pores with same pore diameter (0.74 mm) (b) 2D image of pores with same pore depth (5.20 mm) (c), (d) 3D images of pores with same pore diameter (0.74 mm) and varying pore depths

3.3 Selection of Electrolyte

As a first step to approach the problem, single pore impedance measurements were performed with 6 different concentrations of 3 different electrolytes on a single pore with 1.0 mm diameter and 3.0 mm depth as shown in the Fig. 3.7(a), 3.7(b). The criteria for choosing the best electrolyte was

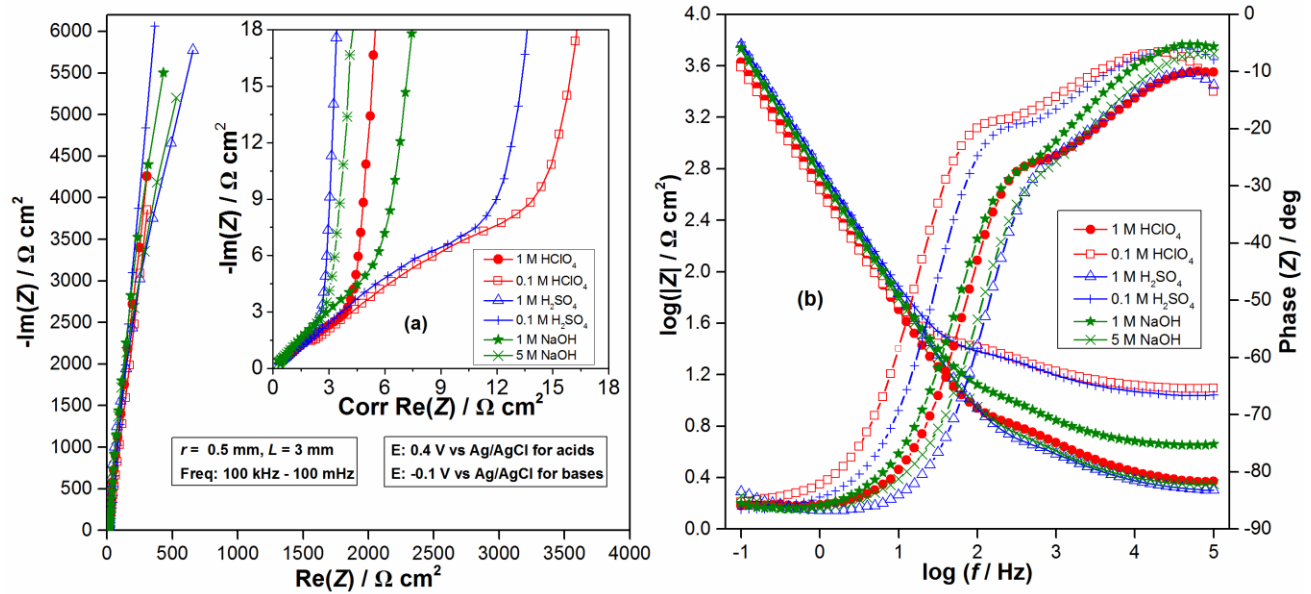


Fig. 3.7 Comparison of electrolytes (a) Nyquist plots (b) Bode Plots

the one which shows the sharpest transition from high frequency to low frequency behaviour in the Nyquist plot (normalised by pore wall area), and where the CPE coefficient was closest to 1, i.e. the one with more ideal capacitive behaviour at low frequency. The α values were evaluated using the graphical method (method 2). 1.0 M H₂SO₄ was deemed the best electrolyte ($\alpha = 0.971$) and showed a sharp transition. The other electrolytes had lower α values, $\alpha = 0.958$ for 5.0 M NaOH, $\alpha = 0.956$ for 1.0 M HClO₄, $\alpha = 0.950$ for 1.0 M NaOH, although all were in acceptable range ($0.9 < \alpha < 1$). Also, the electrolytes with lower concentration, i.e., 0.1 M HClO₄ ($\alpha = 0.942$) and 0.1 M H₂SO₄ ($\alpha = 0.947$) perform poorly compared to high conductivity electrolytes as they

show a significant departure from 45° slope in the high frequency portion and lower CPE coefficients as compared to electrolytes with higher conductivities. Thus, all the subsequent experiments were performed with 1.0 M H₂SO₄. Next, the effect of varying pore depth, pore radii, number of pores (pore density) and electrolyte conductivity is discussed.

3.4 Pore Depth Variation

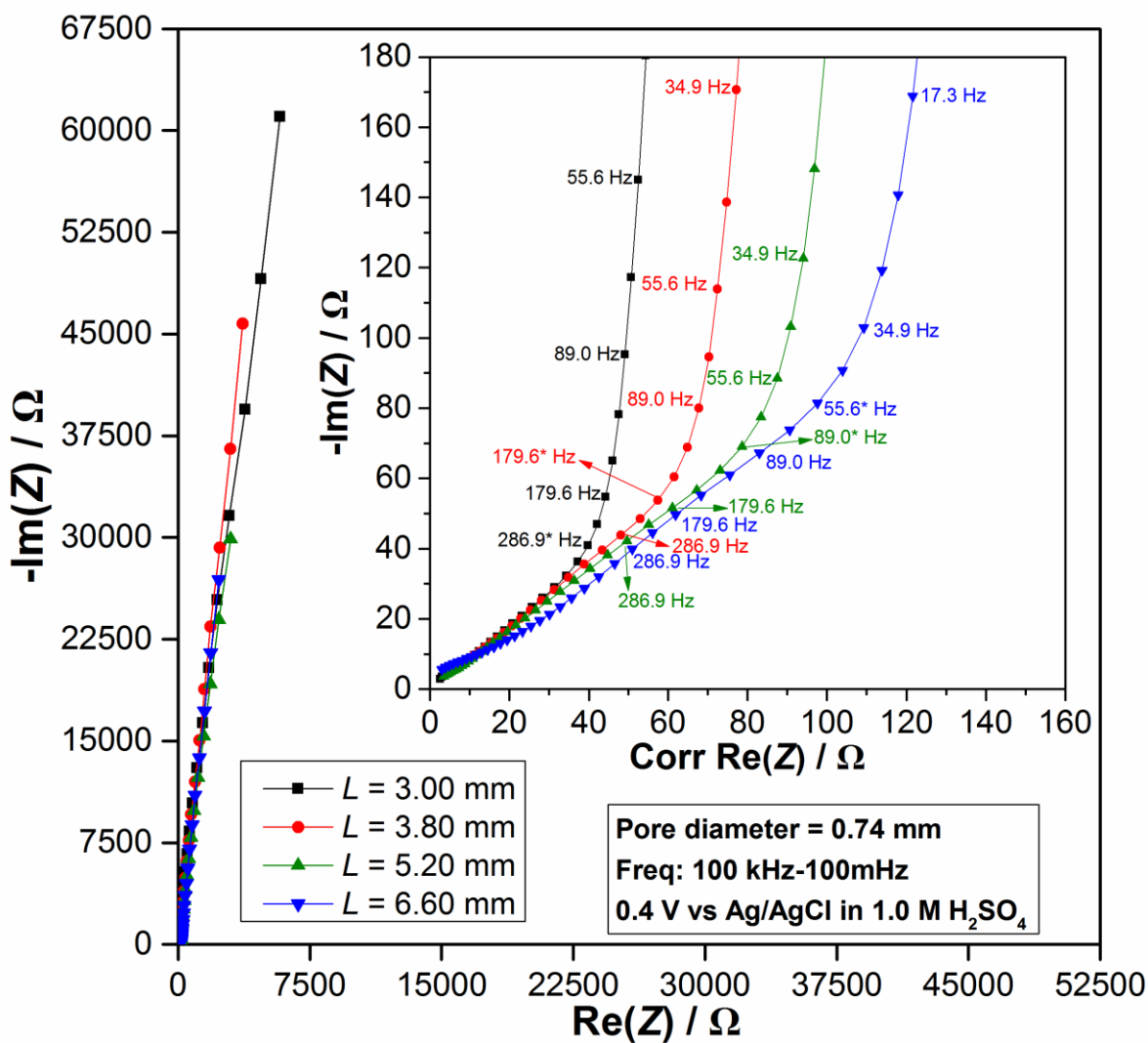


Fig. 3.8 Nyquist plots for effect of varying pore depth (Single pore)

Fig. 3.8 shows the Nyquist plot of pore depth variation for a single pore with increasing aspect ratios (L/D) varying from 4.04 ($L = 3.00$ mm) to 8.89 ($L = 6.60$ mm) with a constant pore diameter ($D = 0.74$ mm) in 1.0 M H_2SO_4 solution. It can be seen from the inset of Fig. 3.8 that as the pore depth is increased, the transition frequency (marked by *) shifts to lower frequencies. As the frequency is decreased from high to low frequencies, the equipotential lines to which the electroactive ions can penetrate move from the orifice to the pore bottom. [40,66]. At very high frequencies, based on Eq. (3), penetration depth of the ac signal is very small compared to the pore depth ($\lambda \ll L$), and the ac signal cannot enter deeply into the pore because of the IR drop and a very low impedance of the pore walls. On the other hand, at much lower frequencies, $\lambda \gg L$, and the ac signal can penetrate to the bottom of the pore [36]. Hence, the whole pore wall area, including the bottom of the pore, becomes electrochemically accessible [34,45,56]. In other words, if all other geometrical (r , pore density) and electrochemical parameters (C_{dl} , K) are constant, a deeper pore requires lower frequencies to access the whole pore volume [55]. In addition, the absolute value of impedance in the low frequency range decreases with the increase of pore depth simply because surface area of inner pore wall increases with the pore depth increase.

Table 3.1 Change of the pore depth on transition frequency

	Pore Depth (L) mm	Transition Frequency (f_t) Hz	$(L^{n+1}/L^n)^2$	f_t^n/f_t^{n+1}
1	3.00	286.9	-----	-----
2	3.80	179.6	1.604	1.597
3	5.20	89.0	1.873	2.018
4	6.60	55.6	1.611	1.601

An expression for the transition frequency, f_t was obtained by R. Jurczakowski and coworkers [31] by comparing the real parts of asymptotes of high and low frequencies portion of the impedance plot. This expression is given in Eq. (10).

$$\omega_t = \frac{9r}{4\rho L^2 C_{dl}} \quad (10)$$

Here, f_t is related to ω_t by $f_t = \omega_t/2\pi$. Table 3.1 shows the quantitative effect of change of pore depth on the transition frequency. From Eq. (10), the squared ratio of pore depths ($(L^{n+1}/L^n)^2$) should be equal to the ratio of the inverse of the corresponding transition frequencies (f_t^n/f_t^{n+1}). These calculated values are shown in Columns 4 and 5 respectively in Table 3.1, and confirm this within the variability of the measurements. Notably, the transition frequency was obtained by

Table 3.2 Comparison of electrochemical parameters by ZView fit (Method 1 / M1) and Graphical approach (Method 2 / M2) for same pore diameter (0.74 mm) and varying pore depth

Pore Depth (mm)	$R_{\Omega,p}$ (Ω)		C_{pore} (μF)		Q ($\mu F \text{ cm}^{-2} \text{ s}^{\alpha-1}$)		C_{dl} ($\mu F \text{ cm}^{-2}$)		α Dimensionless	
	M1	M2	M1	M2	M1	M2	M1	M2	M1	M2
3.00	128.55	135.49	19.21	16.73	358.42	330.71	274.61	239.27	0.959	0.951
3.80	201.32	200.33	26.53	23.79	384.04	352.39	299.46	268.58	0.958	0.955
5.20	271.69	254.71	39.39	35.34	433.07	389.65	324.91	291.48	0.948	0.947
6.60	348.21	336.20	46.62	40.71	390.35	343.74	302.96	264.59	0.949	0.949
							300.48	265.98	0.954	0.951
							± 20.60	± 21.38	± 0.006	± 0.003

choosing the experimentally measured frequency in the middle of the transition zone, and this adds some uncertainty to the reported values.

The distributed resistance and capacitance values for a single pore depth variation obtained by the

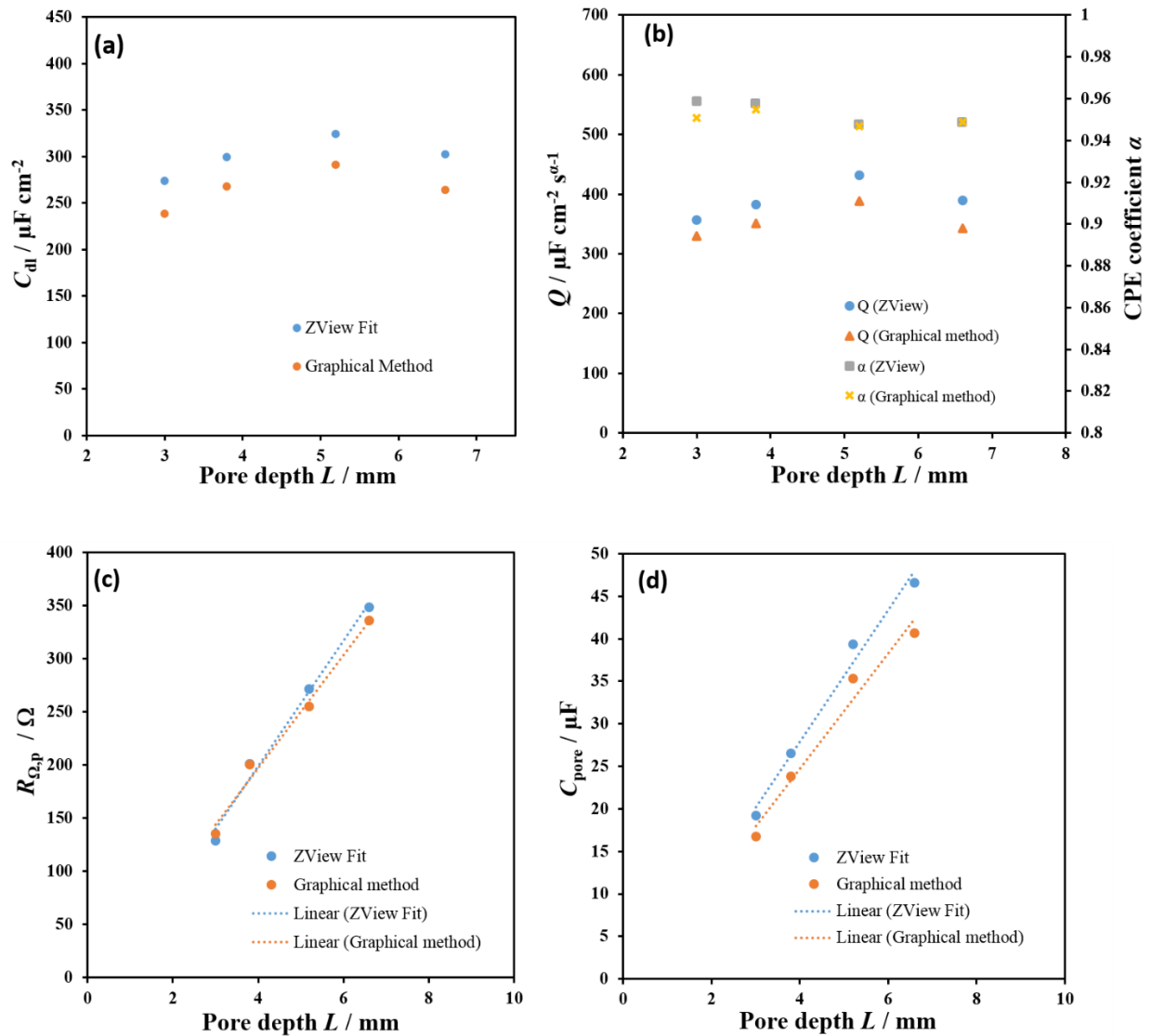


Fig. 3.9 Pore diameter = 0.74 mm (a) Area normalized pore capacitance values vs pore depth (b) CPE parameters Q and α vs pore depth (c) Electrolyte resistance in pores vs pore depth (d) Absolute values of pore capacitance vs pore depth

two methods are summarized in Table 3.2. It shows that the average C_{dl} values obtained by both methods are slightly different with the graphical method giving 12.9% lower values than ZView fitting (method 1) with standard deviations of 6.86% and 8.04% by methods 1 and 2 respectively. Some of the discrepancy between the two methods is due to the fact that method 1 assumes a single α value for the whole frequency range (including the high frequency portion) while method 2 gets the α value only from the low frequency portion. Thus depending on the behavior at high frequency, the two methods may show slightly different values where method 2 is preferred as it is a reliable method of determining capacitance from impedance measurements [67]. However, the $R_{\Omega,p}$ values from method 2 are obtained by linear extrapolation of the low frequency data so that method 1 is likely to be better at estimating this value from an overall least square fitting of the parameters.

Thus, each approach has its limitations. Despite the differences between the two methods, the average α values are comparable: 0.954 ± 0.006 (method 1) vs 0.951 ± 0.003 (method 2) which is also evident from Fig. 3.9(b). The area normalized capacitance values in Table 3.2 have a standard deviation of $< 10\%$ by both methods as mentioned above in this section. This shows that the specific double layer capacitance values are fairly constant (Fig. 3.9(a)) when varying the pore depth as assumed while applying the De Levie's model. As observed in Fig. 3.9(b), the Q values ($\mu\text{F cm}^{-2} \text{s}^{\alpha-1}$) follow a similar trend as C_{dl} .

The plot of $R_{\Omega,p}$ (Ω) vs Pore depth L , or in other words the pore wall area in Fig. 3.9(c) exhibits a linear relationship as described by Eq. (5). Similarly, the plot of C_{pore} (μF) vs Pore depth in Fig. 3.9(d) with C_{pore} defined by $C_{pore} = C_{dl}(2\pi rL)$ [31] also shows a linear relationship confirming that the specific capacitance of our samples is constant. Stated differently, the absolute capacitance scales linearly with the pore depth and the pore wall surface area as expected.

Fig. 3.10 shows the Cyclic Voltammetry (CV) curves for the same set of samples with varying pore depths (single pore) with the current normalized by the respective pore wall area. These CV curves are quasi-rectangular in shape along the current–potential axis without obvious redox peaks. This indicates that all the samples exhibit ideal capacitive behaviour [68,69] when compared at the

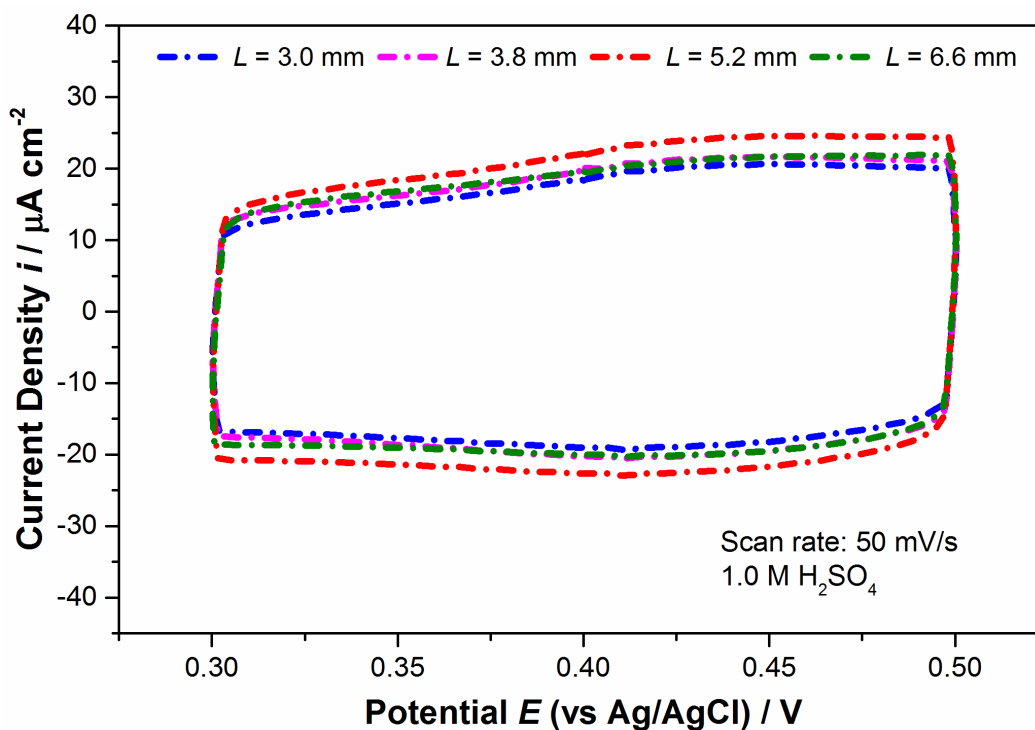


Fig. 3.10 Cyclic Voltammetry curves for pore depth variation for a single pore
(Pore diameter = 0.74 mm)

same scan rate. Further, the total charge (area) enclosed by the CV curves gives a measure of double layer capacitance [70]. Since all the area-normalized curves in Fig. 3.10 look nearly similar, this confirms the specific capacitance of the samples is constant and absolute capacitance of pore wall area increases linearly with the pore depth at a constant pore radius, thus supporting the same observations made by EIS.

The Nyquist plot for pore radii variation for a single pore is shown in Fig. 3.11 wherein the aspect ratio (L/D) is varied from 3.94 ($D = 1.32$ mm) to 11.30 ($D = 0.46$ mm) at a constant pore depth ($L = 5.20$ mm) using 1.0 M H_2SO_4 electrolyte solution. Fig. 3.11 inset shows that the transition frequency (marked by *) shifts to lower frequencies with the decrease of pore radii as the solution resistance in the pores increases with the decrease of cross sectional area [55]. At each frequency, the ac electric signal penetrates pores of different radii to a different extent. Thus, the smaller or narrow pores need lower frequencies than the wider ones for electrochemically accessing all the available surface area [26,40,56,71]. Mathematically Eq. (6) shows $\lambda \propto r^{1/2}$, other parameters remaining constant, a smaller pore radii results in smaller penetration depth as compared to the larger ones at similar frequencies. In addition, large values of impedance seen for smaller pore radii is due to the low surface area of pore walls in this case.

Table 3.3 Change of the pore radii on transition frequency

	Pore Radii (r) mm	Transition Frequency (f_t) Hz	(r^{n+1}/r^n)	f_t^{n+1}/f_t^n
1	0.23	70.4	-----	-----
2	0.33	89.0	1.434	1.261
3	0.37	89.0	1.112	1.000
4	0.51	142.1	1.545	1.601
5	0.66	179.6	1.294	1.264

Similar to the pore depth variation for a single pore, the quantitative effect of pore radii on the transition frequency was investigated. Based on Eq. (10) for the transition frequency, it should scale linearly with the pore radii. Table 3.3 shows the ratio of pore radii and transition frequencies in columns 4 and 5 respectively. The ratio of experimental transition frequencies for two different pore radii is almost the same as the ratio of values of corresponding pore radii, with all other electrode parameters remaining constant. The experimental values of transition frequency for pore radii 0.33 mm and 0.37 mm were found to be equal because of pore radii values being too close. As described by Eq. (10), the transition frequency is expected to be linearly dependent on the pore radius and inversely dependent on the square of the pore depth. This was verified experimentally.

Table 3.4 Comparison of electrochemical parameters by ZView (Method 1 / M1) and Graphical approach (Method 2 / M2) for same pore depth (5.20 mm) and varying pore radii

Pore Radii (mm)	$R_{\Omega,p}$ (Ω)		C_{pore} (μF)		Q ($\mu\text{F cm}^{-2} \text{s}^{\alpha-1}$)		C_{dl} ($\mu\text{F cm}^{-2}$)		α Dimensionless	
	M 1	M2	M1	M2	M1	M2	M1	M2	M1	M2
0.23	917.18	866.84	21.35	20.54	522.59	409.36	279.65	274.97	0.875	0.919
0.33	438.16	418.71	37.36	32.63	464.27	413.81	346.22	302.37	0.941	0.939
0.37	271.69	254.71	39.83	35.34	433.07	389.65	324.91	291.48	0.948	0.947
0.51	139.72	134.57	51.37	47.22	440.78	391.69	309.49	284.49	0.938	0.945
0.66	104.55	94.82	67.49	64.87	431.39	384.44	294.27	300.62	0.944	0.958
							310.91	290.78	0.929	0.942
							± 25.98	± 11.41	± 0.031	± 0.014

The distributed resistance and capacitance values for a single pore radii variation obtained by the two methods are summarized in Table 3.4. In this case, again by employing both methods, the average C_{dl} values fall in the same range (Fig. 3.12(a)) as was the case with pore depth variation with standard deviation of 8.35% and 3.92% by methods 1 and 2 respectively.

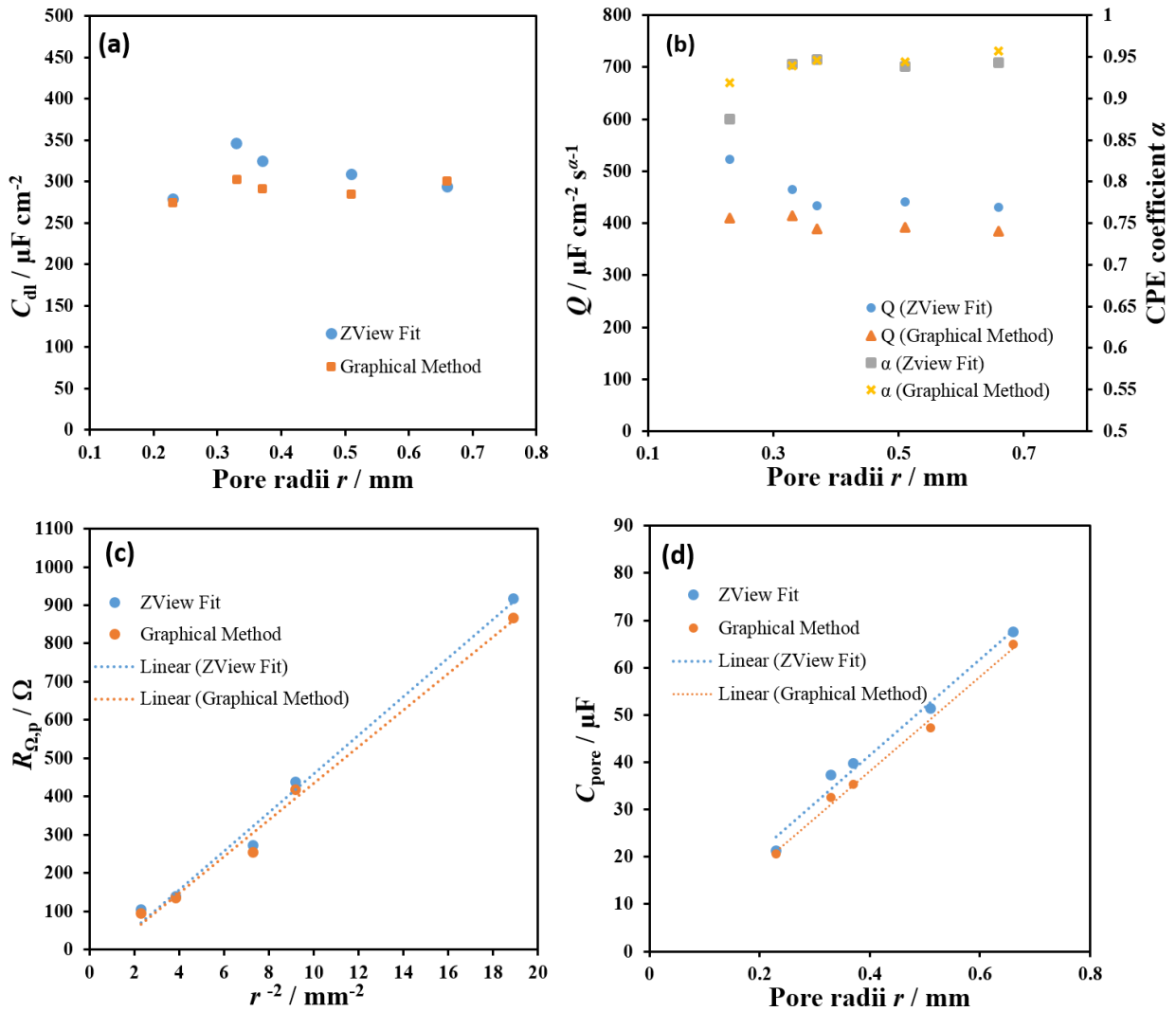


Fig. 3.12 Pore depth = 5.20 mm (a) Area normalized pore capacitance values vs pore radii (b) CPE parameters Q and α vs pore radii (c) Electrolyte resistance in pores vs r^{-2} (d) Absolute values of pore capacitance vs pore radii

A small exception is the smallest pore radii which shows a comparatively lower value of C_{dl} as shown in Table 3.4. This may be because of incomplete wetting of the pore wall area by the electrolyte especially near the bottom of the pores resulting in lower electrochemically accessible surface area. Such a situation is typically observed in narrow pores as the capillary forces oppose the uniform intrusion of the electrolyte. Fig. 3.13 shows the typical CV plots obtained for the same samples at a scan rate of 50 mV/s with the current axis being normalized by the pore wall area. The quasi-rectangular CV curves with the absence of redox peaks indicate the capacitive nature of these samples arising from double layer charging process [68,69]. Nevertheless, these curves confirm once again the specific capacitance of the chosen samples is constant. This minimizes any

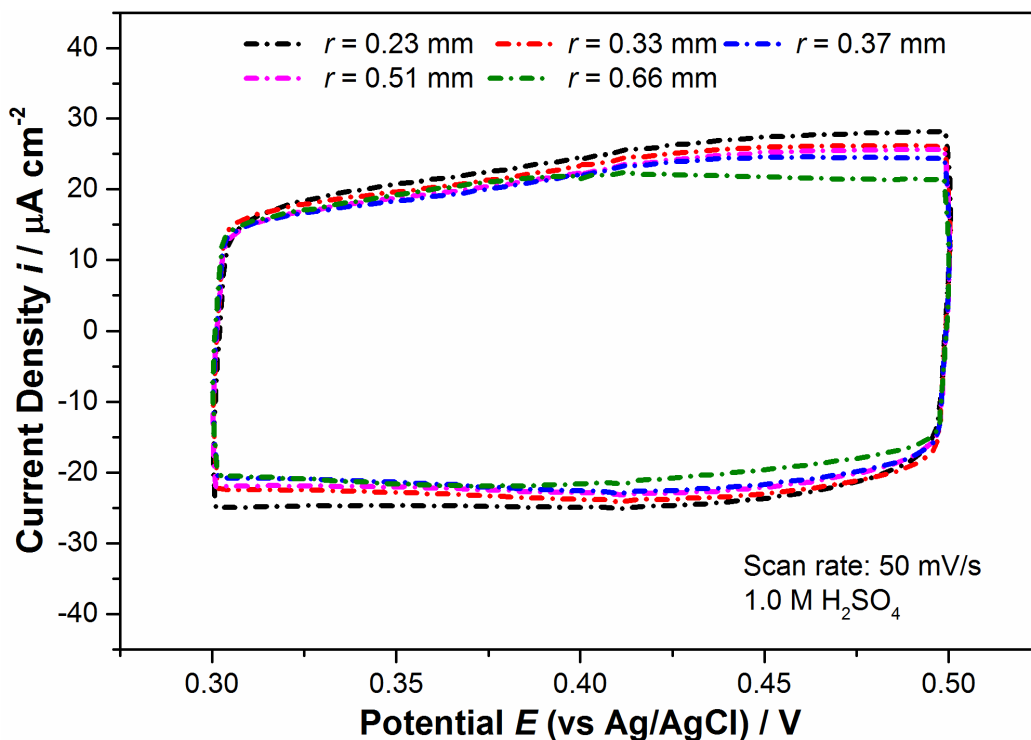


Fig. 3.13 Cyclic Voltammetry curves for pore radii variation for a single pore
(Pore depth = 5.20 mm)

complications arising in our calculated trends due to variation in its values obtained experimentally.

In addition, α values obtained by both methods are comparable and with little variations (standard deviations of 3.34% and 1.48% by methods 1 and 2 respectively), as can be seen from Fig. 3.12(b). It is found that the plot of $R_{\Omega,p}$ (Ω) vs $\frac{1}{r^2}$ in Fig. 3.12(c) exhibits a linear relationship as predicted by Eq. (5) for a constant pore depth. Besides, the plot of C_{pore} (μF) vs pore radii or pore wall surface area shows a linear relationship as seen in Fig. 3.12(d). The reported data exhibit trends for $R_{\Omega,p}$, and C_{pore} which are consistent with the theory, as well as consistent C_{dl} values for our working electrodes using both methods. The relationships obtained above form the basis for verifying the impedance data for a discrete PSD, again with well-defined geometry.

3.6 Uniform Pore Array (Uniform Pore Radii & Depth)

After doing experiments for a single pore depth variation and single pore radii variation, EIS measurements were performed on a single pore, 4 pores and 8 pores with equal pore depth and radii. From the Nyquist plot in Fig. 3.14(a), it can be seen that the absolute value of ohmic corrected impedance for both real and imaginary parts follow the relation in Eq. (11)

$$Z_{1,p} \simeq 4Z_{4,p} \simeq 8Z_{8,p} \quad (11)$$

This is expected because these drilled pores in an electrode can be represented by an equivalent electrical circuit as a parallel combination of single pore impedances [4]. Hence, when evaluating impedance of n single similar pores, $Z_{n,p} = \frac{Z_{1,p}}{n}$. Fig. 3.14(b) shows the impedance normalized by the exposed geometric area ($2\pi rL$) while the Bode plot in Fig. 3.14(c) shows the magnitude of

area normalized absolute values of impedance and phase angle with respect to frequency. As can be seen, the uniform pore arrays normalized by the number of pores have comparable magnitude and phase angles to the single pore experiments. Furthermore, the transition frequency for a pore array of identical pores is the same as it is for a single pore. These results verify the theoretically

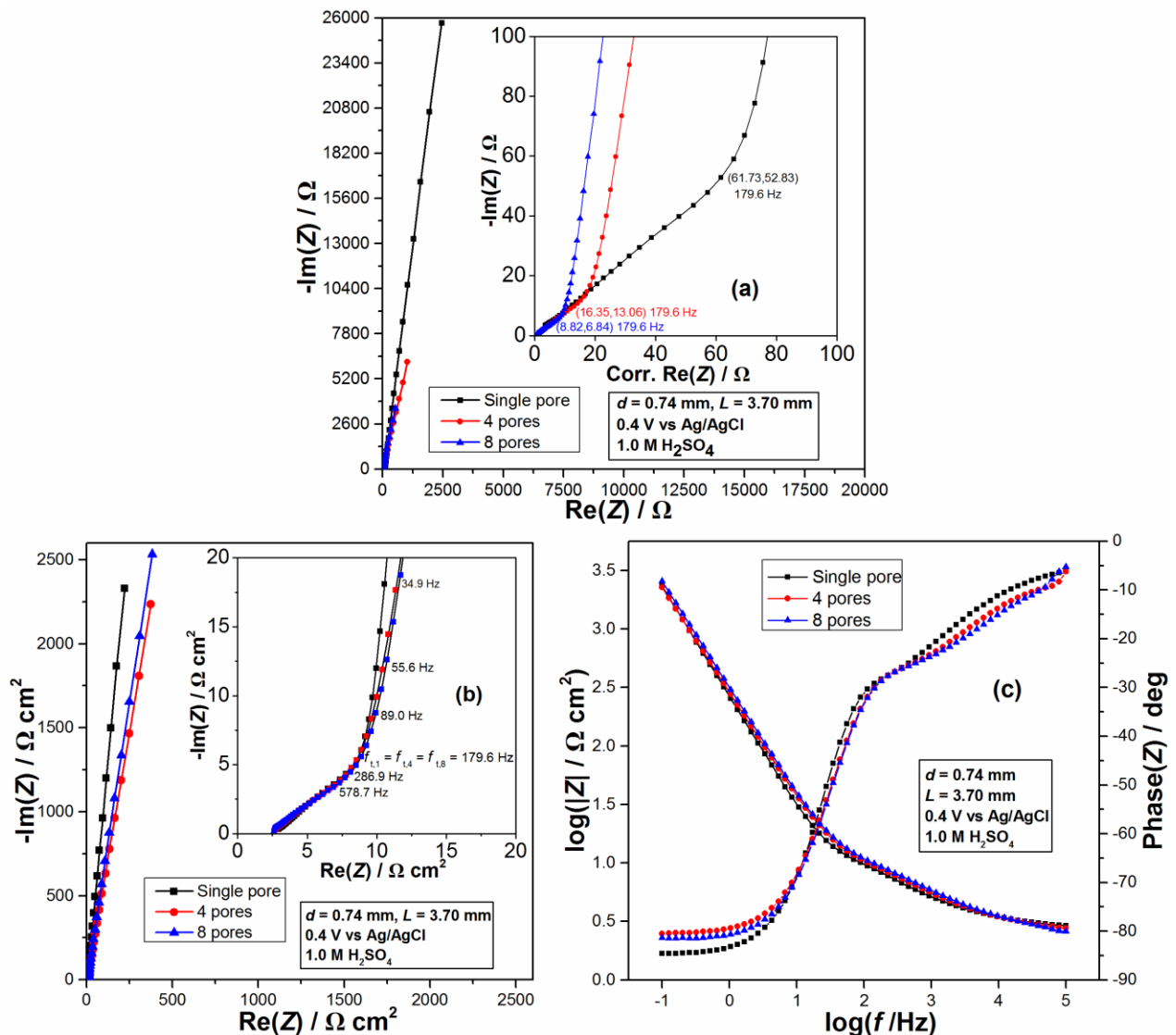


Fig. 3.14 (a) Nyquist plots (absolute values of impedance) (b) Nyquist plots (area normalized impedance) (c) Bode plots for uniform pore arrays

predicted outcome and show that the pores are homogeneous. The corresponding CV curves in Fig. 3.15 with the current axis being area normalized also implies similar specific capacitance values for a single pore and the uniform pore arrays. Before showing the results for different PSD, we briefly look at the effect of varying electrolyte conductivity on the fitted parameters.

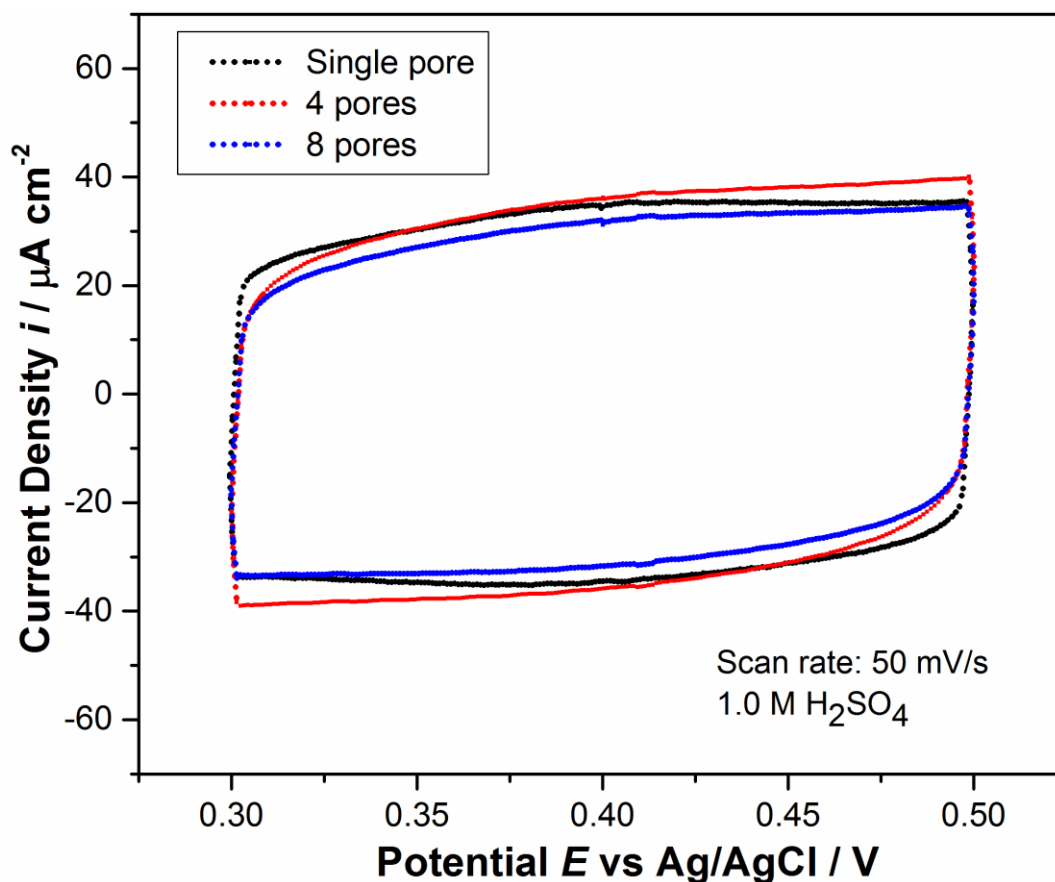


Fig. 3.15 Cyclic Voltammetry curves for uniform pore arrays

3.7 Effect of Electrolyte and Conductivity

From Fig. 3.16, it was clear that higher conductivities gave higher CPE coefficients and a high frequency slope closer to 45° . In order to assess the effect of conductivity and electrolyte composition, the impedance data for a single pore ($d = 1.0$ mm, $L = 3.0$ mm) was fitted using the

ZView software (method 1) for the six electrolytes considered in section 3.3. Fig. 3.16(a) shows the trend of $R_{\Omega,p}$ vs electrolyte resistivity (inverse of conductivity) and this is fairly linear which

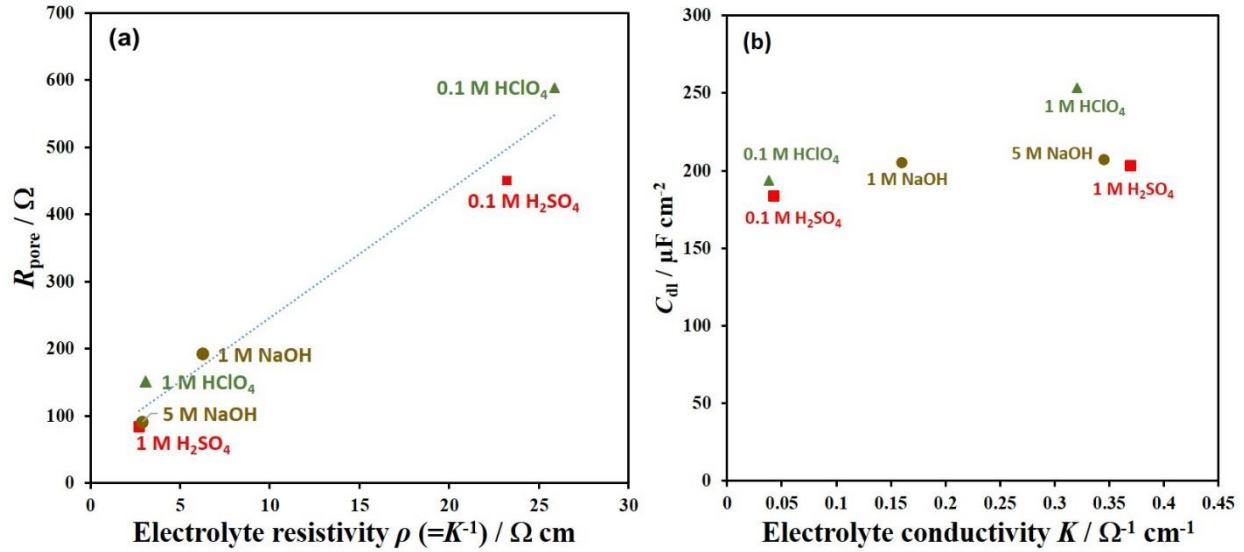


Fig. 3.16 Trend of (a) Electrolyte resistance in pores vs inverse of electrolyte conductivity (b) Area normalized pore capacitance values vs electrolyte conductivity (Pore diameter = 1.0 mm, Depth = 3.0 mm)

should be the case ideally for a constant pore depth and radii. Both the low concentration electrolytes i.e. 0.1 M H₂SO₄ ($K = 0.043 \Omega^{-1}\text{cm}^{-1}$) and 0.1 M HClO₄ ($K = 0.039 \Omega^{-1}\text{cm}^{-1}$) have around 8 times lower conductivity values [72] than 1.0 M H₂SO₄ ($K = 0.369 \Omega^{-1}\text{cm}^{-1}$), 1.0 M HClO₄ ($K = 0.321 \Omega^{-1}\text{cm}^{-1}$), and 5.0 M NaOH ($K = 0.345 \Omega^{-1}\text{cm}^{-1}$), all having conductivities value in the same range. Thus the two lower conductivity electrolytes yield higher values of $R_{\Omega,p}$. From Eq. (5), higher conductivity should yield lower values of $R_{\Omega,p}$ and this is confirmed in Fig. 3.16(a). Besides, the plot of C_{dl} values vs electrolytes conductivity in Fig. 3.16(b) shows that the higher

conductivities give slightly higher values and are almost constant which can be attributed to their CPE coefficients closer to 1, however all electrolytes gave C_{dl} values in the range of 180-250 $\mu\text{F cm}^{-2}$. The concentration of H_2SO_4 was investigated at three different concentrations i.e. 1.0 M, 0.1 M, and 0.01 M to see the effect of a wider range of conductivities on the impedance spectra as well

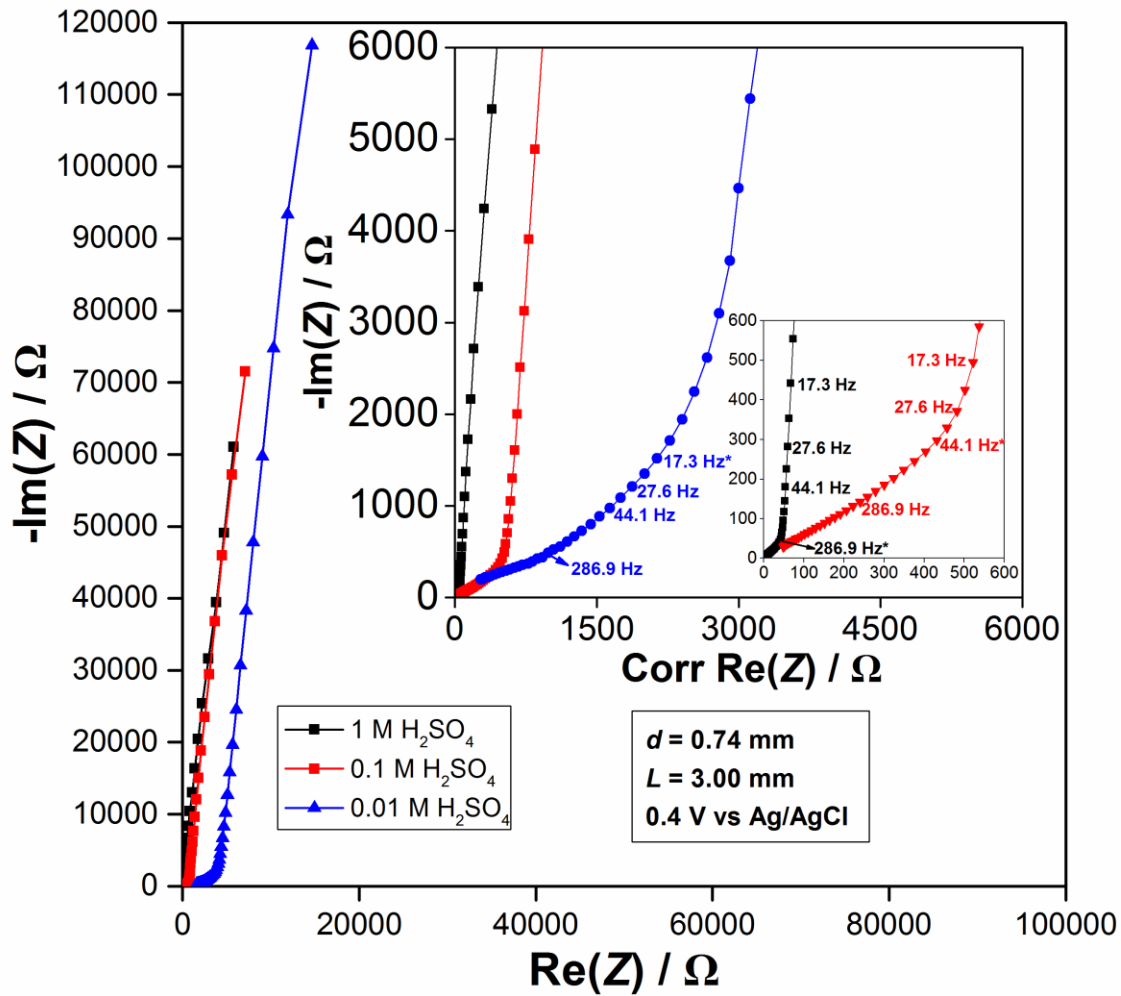


Fig. 3.17 Nyquist Plots for effect of varying electrolyte conductivity (Single pore)

as the fitted parameters. From Ref. [72], the corresponding conductivities are $0.369 \Omega^{-1}\text{cm}^{-1}$ (1.0 M H_2SO_4), $0.043 \Omega^{-1}\text{cm}^{-1}$ (0.1 M H_2SO_4), and $0.006 \Omega^{-1}\text{cm}^{-1}$ (0.01 M H_2SO_4). Nyquist plot in Fig. 3.17 shows that the transition frequency (shown by *) shifts progressively to the lower side as the conductivity of H_2SO_4 is decreased because the solution resistance in the pore increases [55]. The transition frequency in the impedance plot becomes indistinguishable and the length of the high frequency portion is more prolonged as the concentration is decreased by an order of 10. Further, there is significant departure from 45° slope at higher frequencies for lower conductivities, particularly at frequencies above 0.578 kHz for 0.01 M H_2SO_4 solution.

Table 3.5 Summary of electrochemical parameters for varying electrolyte conductivity

Concentration	R_{sol} / Ω	$R_{\Omega, \text{p}} / \Omega$	$Q / \text{F cm}^{-2} \text{ s}^{\alpha-1}$	α	$C_{\text{dl}} / \mu\text{F cm}^{-2}$
1.0 M H_2SO_4	35.72	128.55	0.00035841	0.959	243.80
0.1 M H_2SO_4	209.59	1621.89	0.00033368	0.913	174.07
0.01 M H_2SO_4	1438.16	7183.20	0.00019856	0.906	109.73

The fitted results using ZView are summarised in Table 3.5. Here, it was found that the C_{dl} values drop progressively as the conductivity of H_2SO_4 is lowered, the value for 0.01 M H_2SO_4 solution is only around 45% of the value for 1.0 M H_2SO_4 solution at similar frequencies. A similar trend for C_{dl} values was observed by Bai and Conway [73] in their work on high-area platinized Pt electrodes when the electrolyte conductivity was varied and their model-system electrode behaved like a porous carbon electrode. A plausible explanation to account for this change of C_{dl} values is through Eq. (8) according to which there is very little contribution of the resistive term as its

exponent approaches to 0 as $\alpha \rightarrow 1$ for high α values and small values of the term $(R_{\text{sol}} + R_{\Omega,p}/3)^{(1-\alpha)/\alpha}$. This is the case for high conductivity electrolytes wherein this resistive contribution becomes substantially diminished at sufficiently high conductivities [40], while it is just the opposite for the case of low conductivity electrolytes as seen from the experimental results in Table 3.5. Further, based on the corresponding CVs for 1.0 M H₂SO₄ and 0.1 M H₂SO₄ solutions in Fig. 3.18, the area enclosed by both of them looks quite similar, however Table 3.5 shows the

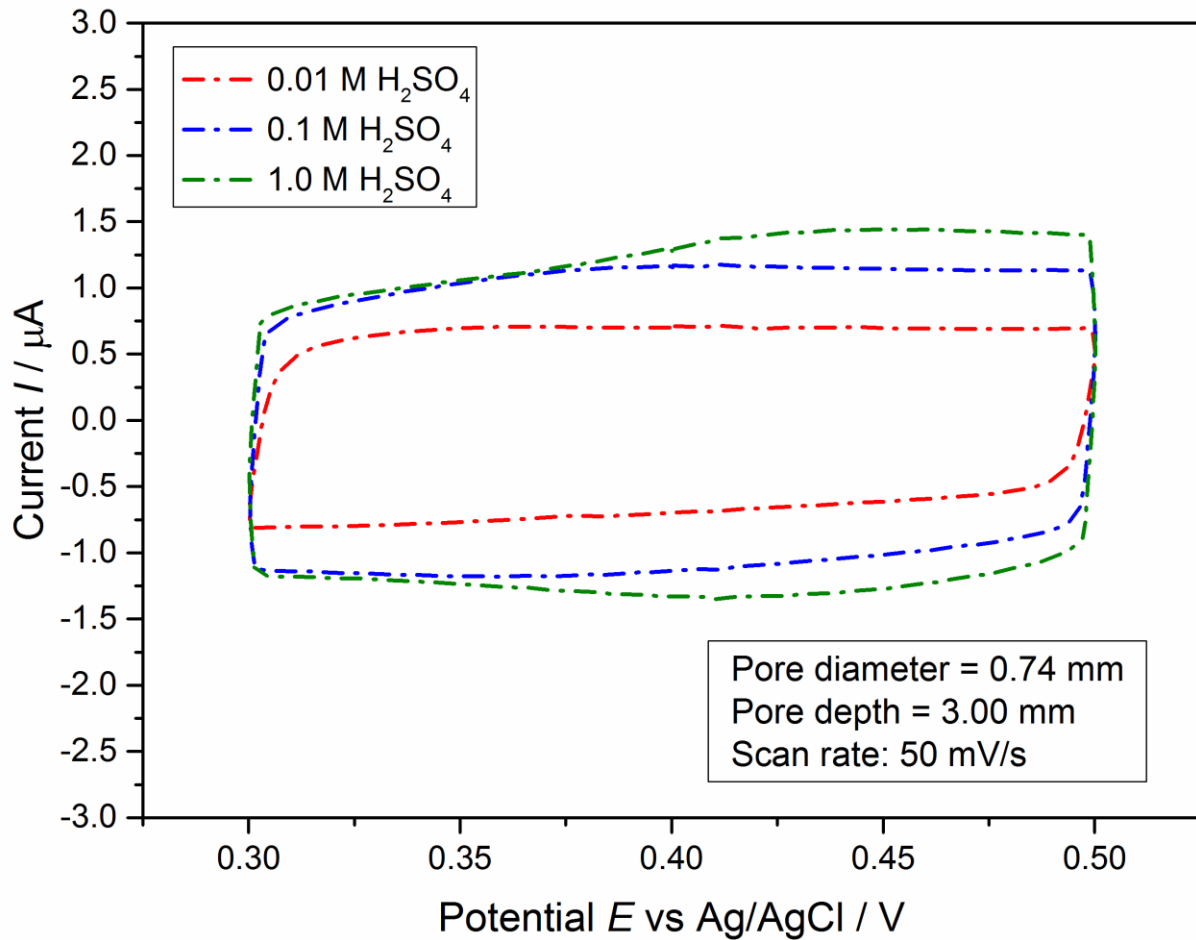


Fig. 3.18 Cyclic Voltammetry curves for effect of varying electrolyte conductivity (single pore)

C_{dl} value for 0.1 M H_2SO_4 solution is around 71% of the value for 1.0 M H_2SO_4 solution at similar frequencies, which clearly shows the role of $R_{\Omega,p}$ and α becomes significant while evaluating C_{dl} values at lower conductivities. In other words, the role of CPE in the equivalent circuit diminishes with higher conductivities and leads to Q values of the same order as C_{dl} . (more ideal capacitive behaviour as $\alpha \rightarrow 1$) In addition, the ionic mobility is larger at higher electrolyte concentration. The higher concentration gradient results in an enhanced mass transfer rate of ions from the bulk solution to the electrode surface during the charging process [74]. The characteristic double layer (diffuse layer) thickness (d), also referred to as the Debye length, can be approximated using the Debye-Hückel parameter (K) given in the following equation [54]:

$$d \approx K^{-1} = \left(\frac{\epsilon_0 \epsilon_r k_B T}{e^2 \sum c_i^0 z_i^2} \right)^{\frac{1}{2}} \quad (12)$$

Here ϵ_0 is the vacuum permittivity, ϵ_r is the relative electrolyte permittivity k_B is the Boltzmann constant, T is the temperature, c_i^0 is the bulk electrolyte concentration, Z_i is the valency of ion i , and e is the elementary charge. Since the ionic properties of the electrolyte, temperature, and the parameters ϵ_0, ϵ_r can be considered constant for the present system, thickness of double layer is inversely related to the square root of concentration.

Thus, a thicker double layer results in lower capacitance value for lower concentrations due to the inverse relationship of the capacitance with the thickness. In other words, the electrolyte of low concentration contains an insufficient number of ions for effective charging of the double layer [74,75] Therefore, the measured capacitance is greater at higher electrolyte conductivities in the case of porous electrodes.

3.8 Pore Size Distributions (PSD)

It was shown in earlier in sections 3.4 and 3.5 that the single pore impedance data for either pore radii or pore depth variation accorded well with the theoretical formula given for evaluating the impedance of a single pore. It was possible because the obtained C_{dl} values were almost constant for the material used in this work. As the procedure of adding single pore impedances worked well for uniform pore arrays, experiments were performed on non-uniform pore arrays, i.e., generated discrete PSD, and a similar procedure was adapted. Mathematically, the single pore impedances were added to give the impedance of a pore array through Eq. (13) and observed how well it compared with the experimental impedance measurements for some non-uniform discrete pore arrays. In Eq. (13) $Z_{p,i}$ is the impedance of i^{th} pore, $Z_{p,\text{total}}$ is the summation of single pore impedances.

$$\frac{1}{Z_{p,\text{total}}} = \sum \frac{1}{Z_{p,i}} \quad (13)$$

Further, for all the cases of PSD considered here, the solution resistance was subtracted from the experimental impedance measurements of single pores and PSD to give only the impedance response of the pores. Firstly, pore arrays with varying pore depths or pore radii were considered. Fig. 3.19(a) shows the Nyquist plot of a pore array with two different pore radii and same pore depth, and vice-versa for Fig. 3.19(b) while Fig. 3.19(c) and Fig. 3.19(d) show slightly more complex pore arrays having same pore depths with three and four different pore radii respectively.

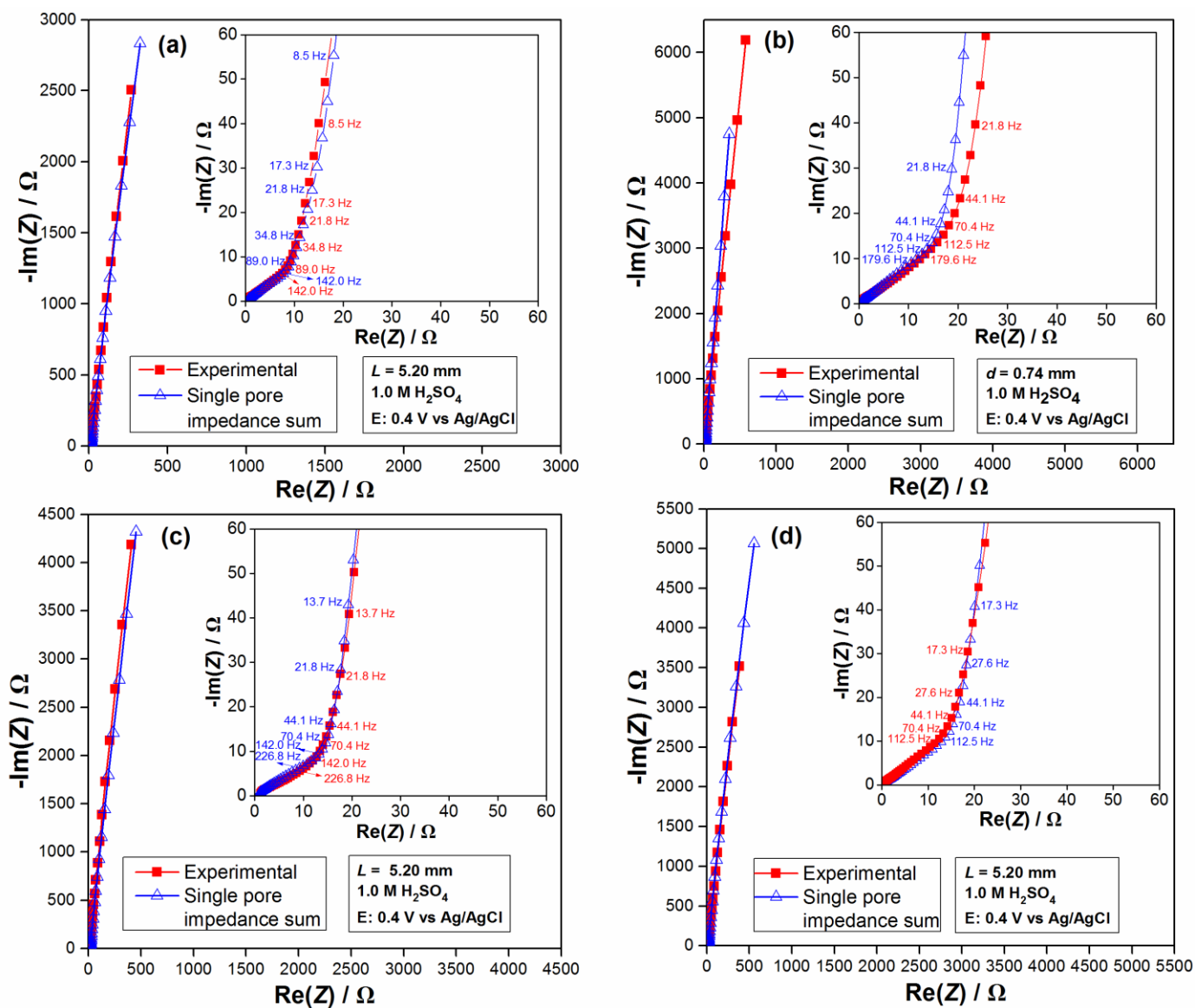


Fig. 3.19 Nyquist plots for four cases of non-uniform pore distributions (a) 6 pore array, 2 different radii: 0.33 mm (3 pores), 0.66 mm

(3 pores) **(b)** 6 pore array, 2 different depths: 3.8 mm (3 pores), 5.2 mm (3 pores) **(c)** 6 pore array, 3 different radii: 0.23 mm (2 pores), 0.33 mm (2 pores), 0.66 mm (2 pores) **(d)** 4 pore array, 4 different radii: 0.33 mm, 0.37 mm, 0.51 mm, 0.66 mm (1 each)

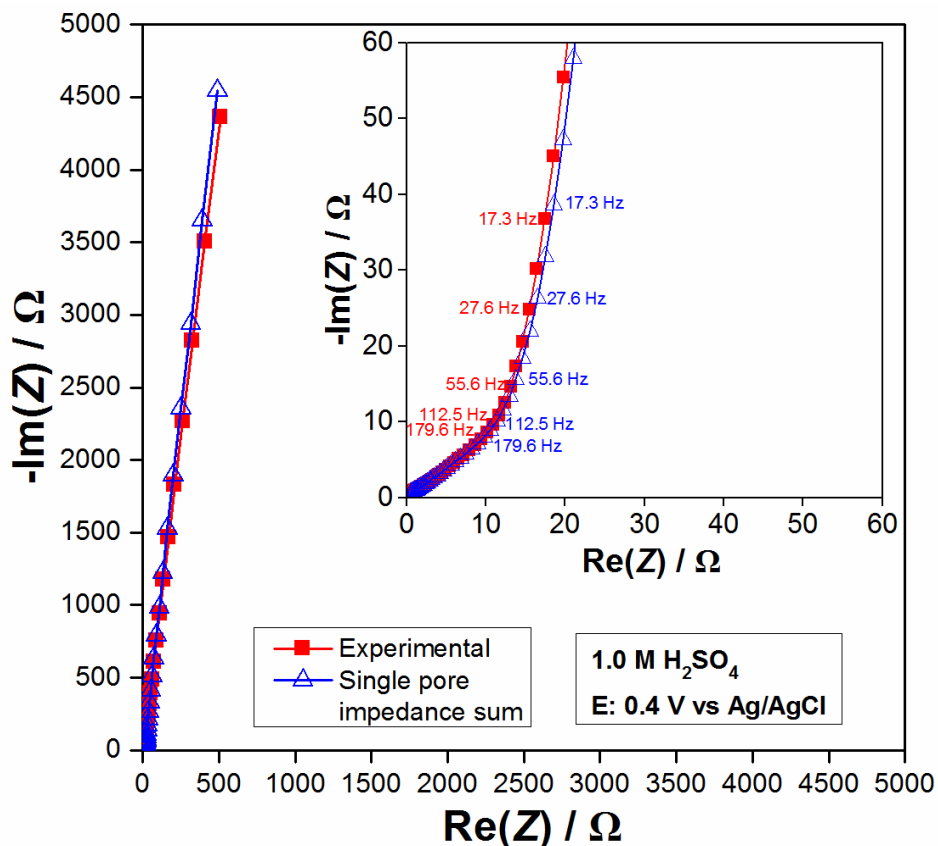


Fig. 3.20 Nyquist plot for a non-uniform pore array: 6 pore array, 3 different radii: 0.23 mm, 0.37 mm, 0.51 mm, 2 different depths: 3.80 mm, 5.20 mm

A pore array with both variable pore depth and pore radii was investigated and the result is shown in Fig. 3.20. This was the most complex PSD considered in this work with three different pore radii and two different pore depths, i.e. six pores that are all different. A good similarity can be

seen between the experimental impedance measurements of the non-uniform pore arrays and the summation of single pore impedance data for all the plots in Fig. 3.19 and Fig. 3.20 over the entire range of frequencies. The comparison is noticeably good for the case of combinatory variable pore depth and radii in Fig. 3.20. All the experimental and single pore impedance summation plots in Fig. 3.19 and Fig. 3.20 look quite similar when compared in the high frequency regime. However little deviation can be seen in the impedance values at low frequencies, which is most likely due to experimental variations.

In addition, it can be concluded from either the sum of single pore equivalent impedance or experimental data for PSD that the transition frequency in Nyquist plots is not clearly distinguishable in value when compared to the single pore impedance plots. This observation can be ascribed to the fact that differently sized pores will have different transition frequencies, hence non-uniformly distributed pore arrangement is expected to show this feature [66].

Thus, the experimental impedance response of pore arrays, both of uniform pore dimensions as well as non-uniform pore dimensions were successfully represented as a sum of experimental impedance response of single pore. This was one of the main objectives of this work along with the confirmation of expected results according to the theory.

3.9 Comment on the nature of CPE behaviour

The exact origin of the dispersion of capacitance noticeable in the porous electrodes is still a matter of debate in the literature. A few works [6,67] found straight line with slopes lower than $\pi/2$ at lower frequencies for a PSD with no faradaic reactions and distribution of double-layer capacity was proposed to be the consequence of distributed pore sizes. However, they ignored the

contribution of the term $(R_{\text{sol}} + R_{\Omega,p}/3)^{(1-\alpha)/\alpha}$ appearing in Eq. (8). After doing the impedance experiments on a single pore followed by uniform pore arrays and non-uniform pore arrays, it seems more plausible that the nature of CPE is due to inhomogeneity along the inner pore walls of the graphite electrode than that of homogeneous inside interface with a distribution of pore sizes. This is supported by the experimental findings of previous works [76–79] since the slope of the high frequency portion for our experimental data is slightly smaller than 45° which cannot be explained by a distribution of pore sizes but by internal inhomogeneity leading to a diminished slope angle by the factor $(1-\alpha)$. According to these works, the microscopic roughness caused CPE behaviour indirectly through energetic inhomogeneities which in turn affected the kinetics of the omnipresent ion adsorption processes [57].

4. Conclusions and Future Work

4.1 Conclusions

In this work, an experimental framework was demonstrated to verify the impedance spectra for progressively complex pore size distributions with well-defined structure. Cylindrical pores were made via drilling on a graphite plate substrate. The experimental EIS measured on the pores exhibited characteristic porous behaviour with a slight deviation from ideal capacitive behavior that could be successfully described by using a CPE element. The experimental data was interpreted using ZView fitting and a graphical approach yielding physically meaningful parameters. The expected behavior from the theory was observed when changing pore depth, pore radii, pore density, and electrolyte conductivity.

Pore arrays, both of uniform pore dimensions and non-uniform pore dimensions, could be successfully represented as a sum of experimental responses of single pores. This approach of modeling pore arrays as a sum of single pores represents an approach to verify the pore impedance for non-uniform ordered pore arrays with well-defined geometry.

4.2 Recommendations for Future Work

The approach demonstrated in this work can be extended to other pore geometries, provided the theoretical formulation for their impedance is known. Recently, a simulation tool [80] was developed to predict diffusive impedance response of several idealized pore geometries with varying cross-sections. In addition, a fast and accurate open-source computational platform [81] exists to characterize big datasets ($>10^8$ voxels) derived from modern tomographic imaging technique. A combination of approaches: large scale tomography and single pore impedance measurements represents a possible approach for characterizing porous materials.

Bibliography

- [1] J. Lee, J. Kim, T. Hyeon, Recent Progress in the Synthesis of Porous Carbon Materials, *Adv. Mater.* 18 (2006) 2073–2094. doi:10.1002/adma.200501576.
- [2] K. Honda, T.N. Rao, D.A. Tryk, A. Fujishima, M. Watanabe, K. Yasui, H. Masuda, Electrochemical Characterization of the Nanoporous Honeycomb Diamond Electrode as an Electrical Double-Layer Capacitor, *J. Electrochem. Soc.* 147 (2000) 659. doi:10.1149/1.1393249.
- [3] O.E. Barcia, E. D’Elia, I. Frateur, O.R. Mattos, N. Pébère, B. Tribollet, Application of the impedance model of de Levie for the characterization of porous electrodes, *Electrochim. Acta.* 47 (2002) 2109–2116. doi:10.1016/S0013-4686(02)00081-6.
- [4] D. Cericola, M.E. Spahr, Impedance Spectroscopic Studies of the Porous Structure of Electrodes containing Graphite Materials with Different Particle Size and Shape, *Electrochim. Acta.* 191 (2016) 558–566. doi:10.1016/j.electacta.2016.01.121.
- [5] J. Chmiola, G. Yushin, R. Dash, Y. Gogotsi, Effect of pore size and surface area of carbide derived carbons on specific capacitance, *J. Power Sources.* 158 (2006) 765–772. doi:10.1016/j.jpowsour.2005.09.008.
- [6] H.-K. Song, H.-Y. Hwang, K.-H. Lee, L.H. Dao, The effect of pore size distribution on the frequency dispersion of porous electrodes, *Electrochim. Acta.* 45 (2000) 2241–2257. doi:10.1016/S0013-4686(99)00436-3.
- [7] N.S.K. Gunda, H.W. Choi, A. Berson, B. Kenney, K. Karan, J.G. Pharoah, S.K. Mitra, Focused ion beam-scanning electron microscopy on solid-oxide fuel-cell electrode: Image analysis and computing effective transport properties, *J. Power Sources.* (2011).

- doi:10.1016/j.jpowsour.2010.12.042.
- [8] A. Du Plessis, S.G. Le Roux, J. Els, G. Booyesen, D.C. Blaine, Application of microCT to the non-destructive testing of an additive manufactured titanium component, Case Stud. Nondestruct. Test. Eval. (2015). doi:10.1016/j.csndt.2015.09.001.
- [9] S. Odaya, R.K. Phillips, Y. Sharma, J. Bellerive, A.B. Phillion, M. Hoorfar, Electrochimica Acta X-ray Tomographic Analysis of Porosity Distributions in Gas Diffusion Layers of Proton Exchange Membrane Fuel Cells, Electrochim. Acta. 152 (2015) 464–472. doi:10.1016/j.electacta.2014.11.143.
- [10] S. Hasanpour, M. Hoorfar, A.B. Phillion, Electrochimica Acta Different Methods for Determining Porosity of Gas Diffusion Layer using X-ray Microtomography, Electrochim. Acta. 185 (2015) 34–39. doi:10.1016/j.electacta.2015.10.083.
- [11] Z. Fishman, J. Hinebaugh, A. Bazylak, Microscale Tomography Investigations of Heterogeneous Porosity Distributions of PEMFC GDLs, J. Electrochem. Soc. (2010). doi:10.1149/1.3481443.
- [12] P. Fievet, M. Mullet, J. Pagetti, Impedance measurements for determination of pore texture of a carbon membrane, J. Memb. Sci. 149 (1998) 143–150. doi:10.1016/S0376-7388(98)00186-0.
- [13] M.G. Sullivan, R. Kötz, O. Haas, Thick active layers of electrochemically modified glassy carbon electrochemical impedance studies, J. Electrochem. Soc. 147 (2000) 308–317. doi:10.1149/1.1393192.
- [14] K. Honda, T.N. Rao, D.A. Tryk, A. Fujishima, M. Watanabe, K. Yasui, H. Masuda, Impedance Characteristics of the Nanoporous Honeycomb Diamond Electrodes for Electrical Double-Layer Capacitor Applications, J. Electrochem. Soc. 148 (2001) A668.

- doi:10.1149/1.1373450.
- [15] H.-K. Song, J.-H. Sung, Y.-H. Jung, K.-H. Lee, L.H. Dao, M.-H. Kim, H.-N. Kim, Electrochemical Porosimetry, *J. Electrochem. Soc.* 151 (2004) E102.
doi:10.1149/1.1641041.
- [16] C. Punckt, M.A. Pope, I.A. Aksay, On the electrochemical response of porous functionalized graphene electrodes, *J. Phys. Chem. C.* 117 (2013) 16076–16086.
doi:10.1021/jp405142k.
- [17] H.D. Yoo, J.H. Jang, J.H. Ryu, Y. Park, S.M. Oh, Impedance analysis of porous carbon electrodes to predict rate capability of electric double-layer capacitors, *J. Power Sources.* 267 (2014) 411–420. doi:10.1016/j.jpowsour.2014.05.058.
- [18] E. Barsoukov, J.R. Macdonald, *Impedance Spectroscopy: Theory, Experiment, and Applications*, John Wiley & Sons, Inc., Hoboken, NJ, USA, 2005.
doi:10.1002/0471716243.
- [19] X.-Z. Yuan, C. Song, H. Wang, J. Zhang, *Electrochemical Impedance Spectroscopy in PEM Fuel Cells*, Springer London, London, 2010. doi:10.1007/978-1-84882-846-9.
- [20] K. Jüttner, Electrochemical impedance spectroscopy (EIS) of corrosion processes on inhomogeneous surfaces, *Electrochim. Acta.* 35 (1990) 1501–1508. doi:10.1016/0013-4686(90)80004-8.
- [21] H.T. Zheng, Y. Li, S. Chen, P.K. Shen, Effect of support on the activity of Pd electrocatalyst for ethanol oxidation, *J. Power Sources.* (2006).
doi:10.1016/j.jpowsour.2006.09.062.
- [22] L. Yu, Z. Wang, L. Shi, S. Yuan, Y. Zhao, J. Fang, W. Deng, Photoelectrocatalytic performance of TiO₂ nanoparticles incorporated TiO₂ nanotube arrays, *Appl. Catal. B*

- Environ. 113–114 (2012) 318–325. doi:10.1016/j.apcatb.2011.12.004.
- [23] F. Hilario, V. Roche, A. Moreira, J. Junior, R. Pereira, *Electrochimica Acta* Application of the transmission line model for porous electrodes to analyse the impedance response of TiO₂ nanotubes in physiological environment, *Electrochim. Acta.* 253 (2017) 599–608. doi:10.1016/j.electacta.2017.09.045.
- [24] J. Bisquert, F. Fabregat-santiago, S. Ferriols, P. Bogdanoff, E.C. Pereira, S.P. Brazil, Doubling Exponent Models for the Analysis of Porous Film Electrodes by Impedance . Relaxation of TiO₂ Nanoporous in Aqueous Solution, (2000) 2287–2298. doi:10.1021/jp993148h.
- [25] W. Shi, *Fitting impedance spectra and calculations of penetration depth*, University of Massachusetts Boston, 2009.
<http://ezproxy.library.ubc.ca/login?url=https://search.proquest.com/docview/305137010?accountid=14656>.
- [26] D. Qu, *Studies of the activated carbons used in double-layer supercapacitors*, *J. Power Sources.* 109 (2002) 403–411. doi:10.1016/S0378-7753(02)00108-8.
- [27] T.-C. Weng, H. Teng, *Characterization of High Porosity Carbon Electrodes Derived from Mesophase Pitch for Electric Double-Layer Capacitors*, *J. Electrochem. Soc.* (2001). doi:10.1149/1.1357171.
- [28] S. Il Pyun, C.H. Kim, S.W. Kim, J.H. Kim, *Effect of Pore Size Distribution of Activated Carbon Electrodes on Electric Double-Layer Capacitor Performance*, *J. New Mater. Electrochem. Syst.* (2002) 289–285. doi:10.1007/978-94-007-7076-8.
- [29] J.-P. Candy, P. Fouilloux, M. Keddam, H. Takenouti, *The characterization of porous electrodes by impedance measurements*, *Electrochim. Acta.* 26 (1981) 1029–1034.

- doi:10.1016/0013-4686(81)85072-4.
- [30] F. La Mantia, J. Vetter, P. Novák, Impedance spectroscopy on porous materials: A general model and application to graphite electrodes of lithium-ion batteries, *Electrochim. Acta.* 53 (2008) 4109–4121. doi:10.1016/j.electacta.2007.12.060.
- [31] R. Jurczakowski, C. Hitz, A. Lasia, Impedance of porous Au based electrodes, *J. Electroanal. Chem.* 572 (2004) 355–366. doi:10.1016/j.jelechem.2004.01.008.
- [32] H. Keiser, K.D. Beccu, M.A. Gutjahr, Abschätzung der porenstruktur poröser elektroden aus impedanzmessungen, *Electrochim. Acta.* 21 (1976) 539–543. doi:10.1016/0013-4686(76)85147-X.
- [33] K. Eloot, F. Debuyck, M. Moors, A.P. Van Peteghem, Calculation of the impedance of noncylindrical pores Part I: Introduction of a matrix calculation method, *J. Appl. Electrochem.* 25 (1995) 326–333. doi:10.1007/BF00249650.
- [34] K. Eloot, F. Debuyck, M. Moors, A.P. Van Peteghem, Calculation of the impedance of noncylindrical pores Part II: Experimental verification on pores drilled into stainless steel, *J. Appl. Electrochem.* 25 (1995) 334–339. doi:10.1007/BF00249651.
- [35] G.J. Lee, S. Il Pyun, C.H. Kim, Kinetics of double-layer charging/discharging of the activated carbon fiber cloth electrode: Effects of pore length distribution and solution resistance, *J. Solid State Electrochem.* 8 (2004) 110–117. doi:10.1007/s10008-003-0392-x.
- [36] A. Lasia, *Electrochemical Impedance Spectroscopy and its Applications*, 2002. doi:10.1007/0-306-46916-2_2.
- [37] L.M. Gassa, J.R. Vilche, M. Ebert, K. Jüttner, W.J. Lorenz, Electrochemical impedance spectroscopy on porous electrodes, *J. Appl. Electrochem.* 20 (1990) 677–685.

- doi:10.1007/BF01008882.
- [38] Z. Stojek, The Electrical Double Layer and Its Structure, in: *Electroanal. Methods*, Springer Berlin Heidelberg, Berlin, Heidelberg, 2010: pp. 3–9. doi:10.1007/978-3-642-02915-8_1.
- [39] J.A. Lim, N.S. Park, J.S. Park, J.H. Choi, Fabrication and characterization of a porous carbon electrode for desalination of brackish water, *Desalination*. 238 (2009) 37–42. doi:10.1016/j.desal.2008.01.033.
- [40] B.E. Conway, *Electrochemical Supercapacitors: Scientific Fundamentals and Technological Application*, Kluwer Academic/Plenum Publishers, New York, 1999. doi:10.15713/ins.mmj.3.
- [41] M. Winter, R.J. Brodd, What are batteries, fuel cells, and supercapacitors?, *Chem. Rev.* 104 (2004) 4245–4269. doi:10.1021/cr020730k.
- [42] P. Simon, Y. Gogotsi, Materials for electrochemical capacitors, *Nat. Mater.* 7 (2008) 845–854. doi:10.1038/nmat2297.
- [43] D.D. Macdonald, Reflections on the history of electrochemical impedance spectroscopy, *Electrochim. Acta.* 51 (2006) 1376–1388. doi:10.1016/j.electacta.2005.02.107.
- [44] H. Cesiulis, N. Tsyntaru, A. Ramanavicius, G. Ragoisha, *Nanostructures and Thin Films for Multifunctional Applications*, 2016. doi:10.1007/978-3-319-30198-3.
- [45] R. de Levie, On porous electrodes in electrolyte solutions. I. Capacitance effects, *Electrochim. Acta.* 8 (1963) 751–780. doi:10.1016/0013-4686(63)80042-0.
- [46] R. de Levie, On porous electrodes in electrolyte solutions, *Electrochim. Acta.* 8 (1963) 751–780. doi:10.1016/0013-4686(63)80042-0.
- [47] I.D. Raistrick, Impedance studies of porous electrodes, *Electrochim. Acta.* 35 (1990)

- 1579–1586. doi:10.1016/0013-4686(90)80013-E.
- [48] P. Agarwal, Measurement Models for Electrochemical Impedance Spectroscopy, J. Electrochem. Soc. (1992). doi:10.1149/1.2069522.
- [49] C. Hitz, A. Lasia, Experimental study and modeling of impedance of the her on porous Ni electrodes, J. Electroanal. Chem. 500 (2001) 213–222. doi:10.1016/S0022-0728(00)00317-X.
- [50] E. Frackowiak, F. Béguin, Carbon materials for the electrochemical storage of energy in capacitors, Carbon N. Y. 39 (2001) 937–950. doi:10.1016/S0008-6223(00)00183-4.
- [51] M.E. Suss, T.F. Baumann, M.A. Worsley, K.A. Rose, T.F. Jaramillo, M. Stadermann, J.G. Santiago, Impedance-based study of capacitive porous carbon electrodes with hierarchical and bimodal porosity, J. Power Sources. 241 (2013) 266–273. doi:10.1016/j.jpowsour.2013.03.178.
- [52] O.K. Varghese, P.D. Kichambre, D. Gong, K.G. Ong, E.C. Dickey, C.A. Grimes, Gas sensing characteristics of multi-wall carbon nanotubes, Sensors Actuators, B Chem. 81 (2001) 32–41. doi:10.1016/S0925-4005(01)00923-6.
- [53] H. Song, H. Song, Y. Jung, Y. Jung, K. Lee, K. Lee, L.H. Dao, L.H. Dao, Electrochemical impedance spectroscopy of porous electrodes: the effect of pore size distribution, Electrochim. Acta. 44 (1999) 3513–3519. doi:10.1016/S0013-4686(99)00121-8.
- [54] A.J. Bard, L.R. Faulkner, ELECTROCHEMICAL METHODS Fundamentals and Applications, 2nd Editio, John Wiley & Sons, Inc., New York, 2001.
- [55] M. Itagaki, S. Suzuki, I. Shitanda, K. Watanabe, H. Nakazawa, Impedance analysis on electric double layer capacitor with transmission line model, J. Power Sources. 164 (2007) 415–424. doi:10.1016/j.jpowsour.2006.09.077.

- [56] C. Yang, C.-Y. Vanessa Li, F. Li, K.-Y. Chan, Complex Impedance with Transmission Line Model and Complex Capacitance Analysis of Ion Transport and Accumulation in Hierarchical Core-Shell Porous Carbons, *J. Electrochem. Soc.* 160 (2013) H271–H278. doi:10.1149/2.016306jes.
- [57] T. Pajkossy, R. Jurczakowski, Electrochemical impedance spectroscopy in interfacial studies, (2017) 53–58. doi:10.1016/j.coelec.2017.01.006.
- [58] J. Bisquert, G. Garcia-Belmonte, F. Fabregat-Santiago, A. Compte, Anomalous transport effects in the impedance of porous film electrodes, *Electrochem. Commun.* 1 (1999) 429–435. doi:10.1016/S1388-2481(99)00084-3.
- [59] J. Bisquert, Influence of the boundaries in the impedance of porous film electrodes, *Phys. Chem. Chem. Phys.* (2000). doi:10.1039/b001708f.
- [60] G.J. Brug, A.L.G. van den Eeden, M. Sluyters-Rehbach, J.H. Sluyters, The analysis of electrode impedances complicated by the presence of a constant phase element, *J. Electroanal. Chem.* 176 (1984) 275–295. doi:10.1016/S0022-0728(84)80324-1.
- [61] M.E. Orazem, N. Pébère, B. Tribollet, Enhanced Graphical Representation of Electrochemical Impedance Data, *J. Electrochem. Soc.* 153 (2006) B129. doi:10.1149/1.2168377.
- [62] D. Wang, F. Li, H. Fang, M. Liu, G. Lu, H. Cheng, Effect of Pore Packing Defects in 2-D Ordered Mesoporous Carbons on Ionic Transport Effect of Pore Packing Defects in 2-D Ordered Mesoporous Carbons on Ionic Transport, (2006) 86–88. doi:10.1021/jp0572683.
- [63] P.L. Taberna, P. Simon, J.F. Fauvarque, Electrochemical Characteristics and Impedance Spectroscopy Studies of Carbon-Carbon Supercapacitors, *J. Electrochem. Soc.* 150 (2003) A292. doi:10.1149/1.1543948.

- [64] M. Lefebvre, Z. Qi, D. Rana, P.G. Pickup, Chemical Synthesis, Characterization, and Electrochemical Studies of Poly(3,4-ethylenedioxythiophene)/Poly(styrene-4-sulfonate) Composites, *Chem. Mater.* 11 (1999) 262–268. doi:10.1021/cm9804618.
- [65] C. Gabrielli, O. Haas, H. Takenouti, Impedance analysis of electrodes modified with a reversible redox polymer film, *J. Appl. Electrochem.* 17 (1987) 82–90. doi:10.1007/BF01009134.
- [66] S. Pyun, C. Kim, S. Kim, J. Kim, Challenges and Opportunities for the World's Forests in the 21st Century, Springer Netherlands, Dordrecht, 2014. doi:10.1007/978-94-007-7076-8.
- [67] M. Musiani, M. Orazem, B. Tribollet, V. Vivier, Electrochimica Acta Impedance of blocking electrodes having parallel cylindrical pores with distributed radii, *Electrochim. Acta.* 56 (2011) 8014–8022. doi:10.1016/j.electacta.2010.12.004.
- [68] J. Yan, T. Wei, B. Shao, F. Ma, Z. Fan, M. Zhang, C. Zheng, Y. Shang, W. Qian, F. Wei, Electrochemical properties of graphene nanosheet/carbon black composites as electrodes for supercapacitors, *Carbon N. Y.* 48 (2010) 1731–1737. doi:10.1016/j.carbon.2010.01.014.
- [69] S. Numao, K. Judai, J. Nishijo, K. Mizuuchi, N. Nishi, Synthesis and characterization of mesoporous carbon nano-dendrites with graphitic ultra-thin walls and their application to supercapacitor electrodes, *Carbon N. Y.* 47 (2009) 306–312. doi:10.1016/j.carbon.2008.10.012.
- [70] N.L. Torad, R.R. Salunkhe, Y. Li, H. Hamoudi, M. Imura, Y. Sakka, C.-C. Hu, Y. Yamauchi, Electric Double-Layer Capacitors Based on Highly Graphitized Nanoporous Carbons Derived from ZIF-67, *Chem. - A Eur. J.* 20 (2014) 7895–7900.

- doi:10.1002/chem.201400089.
- [71] M.E. Suss, T.F. Baumann, M.A. Worsley, K.A. Rose, T.F. Jaramillo, M. Stadermann, J.G. Santiago, Impedance-based study of capacitive porous carbon electrodes with hierarchical and bimodal porosity, *J. Power Sources*. 241 (2013) 266–273.
doi:10.1016/j.jpowsour.2013.03.178.
- [72] J.A. Dean, LANGE'S HANDBOOK OF CHEMISTRY, *Mater. Manuf. Process*. 5 (1990) 687–688. doi:10.1080/10426919008953291.
- [73] L. Bai, L. Gao, B.E. Conway, Problem of in situ real-area determination in evaluation of performance of rough or porous, gas-evolving electrocatalysts. Part 1.—Basis for distinction between capacitance of the double layer and the pseudocapacitance due to adsorbed H in the H₂ evolution, *J. Chem. Soc., Faraday Trans.* 89 (1993) 235–242.
doi:10.1039/FT9938900235.
- [74] K.L. Yang, S. Yiacoumi, C. Tsouris, Electrosorption capacitance of nanostructured carbon aerogel obtained by cyclic voltammetry, *J. Electroanal. Chem.* 540 (2003) 159–167.
doi:Pii S0022-0728(02)01308-6; Doi 10.1016/S0022-0728(02)01308-6.
- [75] A. Al-Zubaidi, T. Inoue, T. Matsushita, Y. Ishii, S. Kawasaki, Ion adsorption on the inner surface of single-walled carbon nanotubes used as electrodes for electric double-layer capacitors, *Phys. Chem. Chem. Phys.* 14 (2012) 16055–16061. doi:10.1039/c2cp43011h.
- [76] A. Hasbach, U. Retter, K. Siegler, W. Kautek, On the impedance of porous electrodes – double-layer charging and charge transfer on an inhomogeneous inside electrode surface, *J. Electroanal. Chem.* 561 (2004) 29–35. doi:10.1016/j.jelechem.2003.07.017.
- [77] C. Cachet, R. Wiart, The pore texture of zinc electrodes characterized by impedance measurements, *Electrochim. Acta*. 29 (1984) 145–149. doi:10.1016/0013-4686(84)87039-

5.

- [78] T. Pajkossy, Impedance of rough capacitive electrodes, *J. Electroanal. Chem.* 364 (1994) 111–125. doi:10.1016/0022-0728(93)02949-I.
- [79] C.L. Alexander, B. Tribollet, M.E. Orazem, Influence of Micrometric-Scale Electrode Heterogeneity on Electrochemical Impedance Spectroscopy, *Electrochim. Acta.* (2016). doi:10.1016/j.electacta.2016.02.133.
- [80] S.J. Cooper, A. Bertei, D.P. Finegan, N.P. Brandon, Simulated impedance of diffusion in porous media, *Electrochim. Acta.* 251 (2017) 681–689. doi:10.1016/j.electacta.2017.07.152.
- [81] S.J. Cooper, A. Bertei, P.R. Shearing, J.A. Kilner, N.P. Brandon, TauFactor: An open-source application for calculating tortuosity factors from tomographic data, *SoftwareX.* 5 (2016) 203–210. doi:10.1016/j.softx.2016.09.002.